Optical signatures of charge- and energy transfer in TMDC/TMDC and TMDC/perovskite heterostructures

2D Materials

TOPICAL REVIEW

Optical signatures of charge- and energy transfer in TMDC/TMDC and TMDC/perovskite heterostructures

Sarah C Gillespie[1,2,7], Marco van der Laan[3,7], Deepika Poonia[4], Sourav Maiti[5], Sachin Kinge[4,6], Laurens D A Siebbeles[4] and Peter Schall[3,*]

[1] AMOLF Institute, Science Park 104, 1098XG Amsterdam, The Netherlands
[2] TNO Energy Transition, Westerduinweg 3, 1755LE Petten, The Netherlands
[3] Institute of Physics, University of Amsterdam, Science Park 904, 1098XH Amsterdam, The Netherlands
[4] Optoelectronic Materials Section, Department of Chemical Engineering, Delft University of Technology, 2629HZ Delft, The Netherlands
[5] Central Laser Facility, RCaH, STFC-Rutherford Appleton Laboratory, Harwell Science and Innovation Campus, Didcot, United Kingdom
[6] Materials Research & Development, Toyota Motor Europe, B1930 Zaventem, Belgium
[7] Equal contribution.
[*] Author to whom any correspondence should be addressed.

E-mail: p.schall@uva.nl

Keywords: excitons, 2D materials, perovskites, optical spectroscopy, heterostructures

OPEN ACCESS

RECEIVED
13 August 2023

REVISED
28 November 2023

ACCEPTED FOR PUBLICATION
13 March 2024

PUBLISHED
26 March 2024

Abstract

Heterostructures (HSs) based on two-dimensional transition metal dichalcogenides (TMDCs) are highly intriguing materials because of the layers' pronounced excitonic properties and their nontrivial contributions to the HS. These HSs exhibit unique properties that are not observed in either of the constituent components in isolation. Interlayer excitons (IEs), which are electron–hole pairs separated across the HSs, play a central role in determining these HS properties and are of interest both fundamentally and for device applications. In recent years, a major focus has been on understanding and designing HSs composed of two or more TMDC materials. Less attention has been paid to HSs composed of one TMDC layer and a layer of perovskite material. A central challenge in the understanding of HS properties is that basic measurements such as optical spectroscopic analysis can be misinterpreted due to the complexity of the charge transfer dynamics. Addressing these aspects, this review presents an overview of the most common and insightful optical spectroscopic techniques used to study TMDC/TMDC and TMDC/halide perovskite HSs. Emphasis is placed on the interpretation of these measurements in terms of charge transfer and the formation of IEs. Recent advances have started to uncover highly interesting phenomena, and with improved understanding these HSs offer great potential for device applications such as photodetectors and miniaturized optics.

1. Introduction

Two-dimensional (2D) semiconductors and their heterostructures (HSs) are rapidly growing fields of broad interest due to their interesting exciton physics and promising future device applications [1, 2]. These layered materials are strongly bound within the atomic layers, but more weakly bound by Van der Waals forces between layers. In recent years it has become clear that monolayers of transition metal dichalcogenides (TMDCs) exhibit interesting physics due to the combined effects of confinement and reduction of dielectric screening. The latter results in strongly bound excitons, with binding energies of around 500 meV in the monolayer materials [3–5], causing the excitons to be observable at room temperature. The TMDC monolayers typically have optical bandgaps between 1 eV and 3 eV—spanning the near-infrared and visible ranges of the electromagnetic spectrum [3]. However, control over excitons is difficult due to their charge neutrality. Therefore, various ways of influencing and enhancing excitonic behaviour are currently under investigation. Among these, HSs, formed by stacking different monolayer TMDCs, attracted much interest due to their great potential. Various material combinations allow for

more control over the charge carriers in these HSs, while still leveraging the interesting exciton properties of these materials. These properties mean that 2D TMDCs and their HSs have potential applications in high-performance photodetectors and as components of solar cells [6–12].

Interlayer excitons (IEs) are excitons whose charges are spatially separated across the stacked layers of the HS; their observation has garnered justifiable interest within the community [13–16]. Despite their importance for understanding the charge carrier and decay dynamics, interpretation of their experimental signatures remains challenging due to the already rich variety of other excitonic states in these HSs.

In this review, we present a summary of the most common optical spectroscopic tools applied to identify the presence of excitons and their nature in TMDC HSs. These techniques include steady-state photoluminescence (PL) spectroscopy, time-resolved PL (TRPL) spectroscopy, and ultrafast transient absorption (TA) spectroscopy. These key experimental methods, supplemented with additional measurements such as absorption and reflection spectroscopy, Raman spectroscopy, transmission electron microscopy (TEM) and electrical assessment methods, also discussed, can provide important insights into the charge carrier and exciton states and their dynamics within the HS. The synthesis methods of TMDCs and their HSs are a vast topic on their own, for which we refer readers to existing reviews [17–25].

We consider two types of HSs, those composed of purely TMDC layers (TMDC/TMDC) and those with one TMDC monolayer and a layer of semiconducting perovskite materials (TMDC/PMs). We review the experimental insights into the energy- and charge-transfer processes that can occur in TMDC/TMDC and TMDC/PM HSs and how these processes result in the formation of IEs. Because of their complexity and the diverse possibilities of interpretation, several complementary techniques are needed to conclude on the processes at play. Next to true TMDC/TMDC HSs, we also include the investigation of Janus monolayers, for which the chalcogenide layers above and below the metal plane are composed of different chalcogen atoms, and discuss the interpretation of their experimental features.

For the most trustworthy interpretation of the data, it is imperative to consider the different charge carrier recombination pathways that may occur in TMDC HSs and how these can affect the optical properties of the materials. These pathways can arise due to defects, vacancies and grain boundaries within the material, leading to non-radiative recombination. Identifying and differentiating how these pathways might interact, or be confused with charge- and energy-transfer processes is an important issue that is discussed in the final section of this work. Understanding these alternative mechanisms is crucial for an accurate interpretation of the spectroscopic results. The review is structured as follows: starting with a general introduction to the physics of semiconducting TMDCs in section 2, we provide a brief overview of the HS properties and experimental signatures of excitons in TMDC/TMDC HSs in section 3. We then discuss the recent work in mixed TMDC/PM HSs in section 4, before discussing alternative processes in section 5.

2. TMDC monolayers

TMDCs—with chemical formula MX_2, where M is a transition metal and X is a chalcogen atom—can vary from insulators to conductors, depending on their elemental composition and phase. Bulk TMDCs were studied and extensively described decades ago, most notably by Wilson and Yoffe [26], but only came back into focus in 2010 through the seminal work by Mak *et al* [27], after Novoselov *et al* showed it is possible to cleave graphite, and other layered crystals, down to the monolayer with a micromechanical cleavage method [28]. There are several reviews on TMDC monolayers and their HSs, so only a brief classification is given here. For further background, the reader is referred to these earlier reviews [16, 17, 28–30]. The most common configurations for the semiconducting TMDCs are the trigonal prismatic (2H) and the octahedral (1T) phases. These phases differ by the stacking order of the chalcogen on the transition metal atom, as shown in figure 1(a). The 2H phase is stacked in an X–M–X sequence, where the chalcogen atoms are positioned along the same vertical coordinate across different X layers [31], while the 1T phase is stacked in X–M–X' sequence, with the two chalcogen layers displaced from each other.

2.1. Electronic bandstructure

While graphene and the prototypical monolayer TMDCs such as MoS_2 and WSe_2 have a similar honeycomb crystal structure, their optoelectronic properties are vastly different [17]. These properties are determined by the specifics of their electronic bandstructures, which differs significantly between graphene and the TMDCs. The difference roots in two fundamental properties: (i) The heavier transition metals in TMDCs induce strong spin–orbit coupling (SOC), and (ii) the specific two-atom system in the MX_2 (M: Mo, W, X: S, Se) structure breaks inversion symmetry. These fundamental properties of TMDCs result in the opening of a bandgap and the splitting of the K and K' valleys in the electronic bandstructure. Furthermore, a direct-to-indirect bandgap transition results upon stacking several TMDC layers due to specific orbital contributions of the metal and chalcogen atoms, see figure 1(b). Specifically, there are

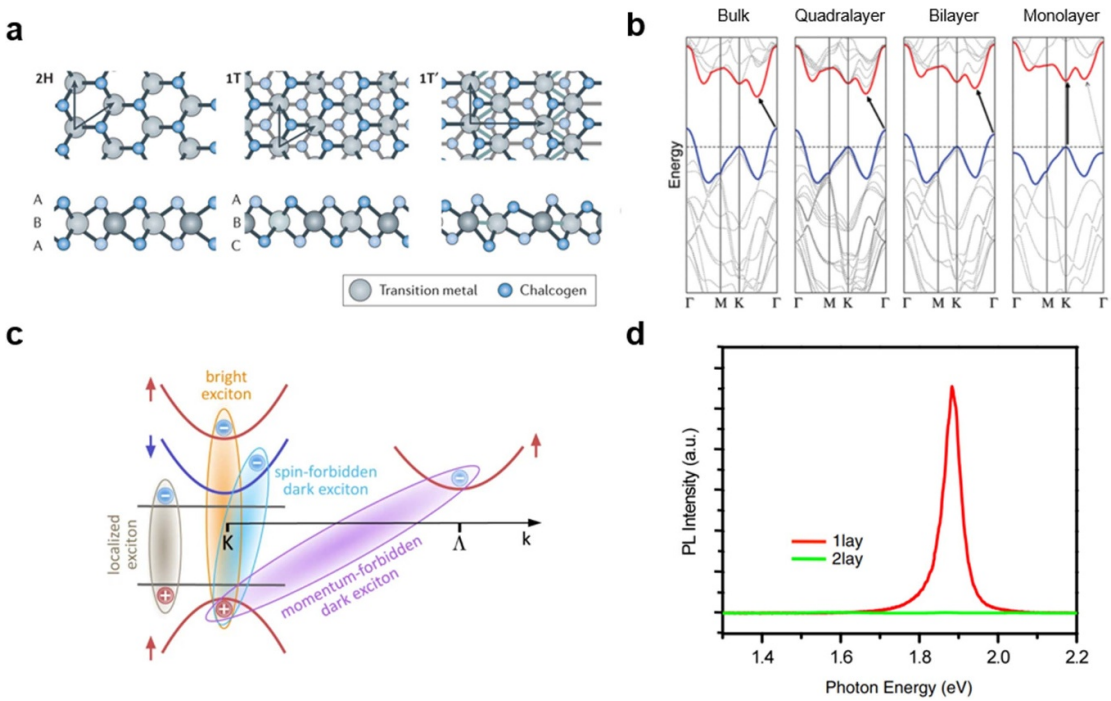

Figure 1. (a) Schematic of a monolayer TMDC with trigonal prismatic, 2*H* (left), distorted octahedral, 1*T* (centre) and dimerized 1*T*″ (right) phases. Reproduced from [31], with permission from Springer Nature. (b) Representation of the electronic bandstructure changes in MoS_2 upon a change in thickness. Reprinted with permission from [44]. Copyright (2010) American Chemical Society. (c) Various possible transitions in TMDCs, showing both optically allowed, and optically forbidden transitions. Reproduced from [16]. CC BY 4.0. (d) Room-temperature photoluminescence spectra of mono- and bi-layer MoS_2, showing the drastic changes induced by layer thickness. Images were adapted from [16, 31, 44] and [27] for (a) to (d), respectively. Reprinted with permission from [27], Copyright (2010) by the American Physical Society.

three valleys of interest in the electronic bandstructure of TMDCs: at the Γ, the *K* and the *K*′ point in the Brillouin zone. A major distinction between the Γ and the *K*-valleys is in the aforementioned relative contributions of the metal and chalcogen orbitals, which cause the direct-to-indirect bandgap crossover due to the more out-of-plane *p*-orbital character of the bands at the Γ and Λ points [32–34]. With increasing number of layers, the states at the Γ point are strongly affected, as shown in figure 1(b). As a result, the prototypical MoS_2, $MoSe_2$, WS_2 and WSe_2 have room-temperature bulk electronic bandgaps of 1.2, 1.1, 1.4 and 1.2 eV, respectively, while their respective monolayers have 2.5, 2.3, 2.6 and 2.2 eV [29, 35]. However, the monolayer values are very sensitive to the measurement geometry and generally, it is more difficult to extract electronic band energies rather than optical bandgap energies, which are related to the excitonic states in these materials.

The distinction between *K* and *K*′ valleys is due to the combined effect of SOC and broken inversion symmetry, causing opposite spins of states in these two valleys [33, 36]. Furthermore, the SOC causes splitting of valence and conduction bands in predominantly these *K* and *K*′ valleys, as shown in figure 1(c) [31]. It was expected that these effects cause perfect spin-valley polarization protected by the above symmetry considerations [37]. However, in practice, the electron–hole exchange interaction causes rapid valley depolarization, even at cryogenic temperatures and in high-quality samples [38, 39]. This suggests that the realization of the often-discussed spin-valleytronics, which aims to use the spin- and valley-degrees of freedom next to the electric charge for solid-state applications, is not very practical in TMDC monolayers. Quantitatively, the energy offsets due to splittings of the valence bands at the *K* points are predicted to be 148, 183, 426 and 456 meV, respectively, for MoS_2, $MoSe_2$, WS_2 and WSe_2 monolayers, while those for the conduction bands are, respectively, 16, 35, 3 and 3 meV [32, 40]. This spin-splitting can render the lowest energetic transition between the valence and conduction band at the *K*-points spin-forbidden, leading to dark states [40]. The existence of these dark states has been shown [41], and it turns out that molybdenum-based dichalcogenides have a spin-allowed lowest transition. In contrast, the lowest transition for tungsten-dichalcogenides is spin-forbidden. This affects the optical properties to a great degree [42, 43].

2.2. Excitons

Another important aspect of the transition from bulk to monolayer is the dielectric screening of electric charges by the material. This screening is drastically reduced from bulk to monolayer, resulting in more strongly bound states of electrons and holes, called excitons [45, 46]. While these bound states also

exist in the bulk, their binding energy is enhanced in monolayers, where it can significantly affect the energetics of the electronic bandstructure. In this case, a simple band model of free carriers is not applicable any more, and ultimately, many of the optoelectronic properties of TMDCs become dominated by the properties of excitons [27]. Experimentally, this manifests as sharp resonances in the optical spectra. At the same time, the symmetry considerations causing the spin-split states still apply. As a result, TMDCs display excitons at the valence and conduction band spin-split states, termed *A* and *B* excitons, respectively, for the lower and higher energy states of the direct ($K \rightarrow K$) bandgap transition [26]. These A and B excitons represent the bright states. Besides these bright states, there might be spin-dark exciton states with energies above or below the bright states, depending on the exchange- and spin–orbit interactions [40]. Moreover, momentum-indirect transitions ($\Gamma \rightarrow \Lambda$, $K \rightarrow \Lambda$) in the bandstructure contribute additional bound states, but optical transitions to these states have much lower oscillator strengths due to the momentum mismatch [16], so they are much less frequently observed. An overview of the possible transitions is given in figure 1(c).

Because of the high exciton binding energies, excited states of the excitons can be experimentally observed. As the excitons are composed of a positively-charged hole and a negatively-charged electron similar to a hydrogen-like atom, their excited states are commonly modelled by a simple Rydberg-like formula. The excited exciton states are then labelled 1*s*, 2*s*, 2*p*, etcetera, following hydrogenic atoms, and they can contribute to the optical spectra. These states lie between the 1*s* excitonic ground state and the continuum band, where the energy difference between these two extremes is called the exciton binding energy. Due to selection rules, however, only the *s* states can be optically excited or probed in the absence of any external fields [47, 48]. Excitingly, recent work suggests that TMDC monolayers show signs of band topology, which would alter the optical selection rules [49]. Mapping out the excited-state energies is one of the common ways of deducing exciton binding energies, as these energies asymptotically approach the continuum band [50].

Finally, in the presence of extra free charges or other excitons, exciton complexes such as trions or biexcitons can form resulting in extra observable states. These extra free charges can occur due to defects, doping or high excitation fluences [51–54], resulting in binding energies in these complexes on the order of 10s of meV, much lower than those of the excitons, yet in some cases high enough to be observed at room temperature. Besides these common excitonic states, many more states can show up in the optical spectra, such as bulk-specific excitons [55], phonon replicas [56, 57], polaritons [58], and defect emission [59], among others. Many of the mentioned phenomena have by now been established in the prototypical Mo- and W-based TMDCs; yet, even in these materials, the richness of the excitonic states makes it difficult to uniquely assign them to spectroscopic features. For the less established TMDCs, compositional changes, such as in the group IV TMDCs (*M*: Hf, Zr; *X*: S, Se), alter the bandstructure [60]. Furthermore, reduced crystal symmetries might cause additional degrees of freedom to appear, such as horizontal linear optical polarization in the case of group VII ReX_2 (*X*: S, Se) compounds [61]. Especially in these less-studied materials, there is still much to discover regarding the nature of their excitonic properties.

2.3. Recombination processes

While there are many excitonic states present, typically only one of them, the lowest allowed transition, is observed in PL spectra at room temperature, see for example figure 1(d). Nevertheless, there are numerous radiative and non-radiative recombination pathways in TMDC monolayers that can affect the average decay rate (figure 2). The dominant pathways can vary depending on the temperature, density and type of defect states present, as well as the applied power density [62]. Under low excitation intensities, exciton–phonon scattering and radiative coupling are the dominant recombination processes. Under higher excitation intensity, exciton–exciton scattering also becomes prominent. One common way of characterising material quality is through PL quantum yield (PLQY) measurements, where low PLQY values indicate that non-radiative dominate over radiative decay channels. Attaining high PLQY in these materials remains a challenge, as a significant fraction of excitons typically recombines non-radiatively via intrinsic trap states, mostly due to chalcogen vacancies [63–66]. This limits the PLQY to an order of 1% (0.1% in MoS_2, 6% in WS_2) and radically minimises the feasible optoelectronic applications of TMDC monolayers [67]. On the other hand, the combined effects of confinement and reduced screening tend to increase light absorption at the exciton lines and enhance the PLQY in monolayers compared to the bulk [16, 27, 44, 68]. Consequently, these 2D materials are strong candidates for applications in next-generation optoelectronic devices [69–72].

Depending on the application in mind, quantum-yield limitations might be overcome by stacking a TMDC monolayer with a material with high quantum efficiency—for example, a perovskite semiconductor. TMDC monolayers can also be stacked with other TMDC monolayers, which can alter the overall excitonic properties of the materials. Naturally, the abundance of phenomena already present in monolayers provides a very versatile platform for material tunability once these monolayers

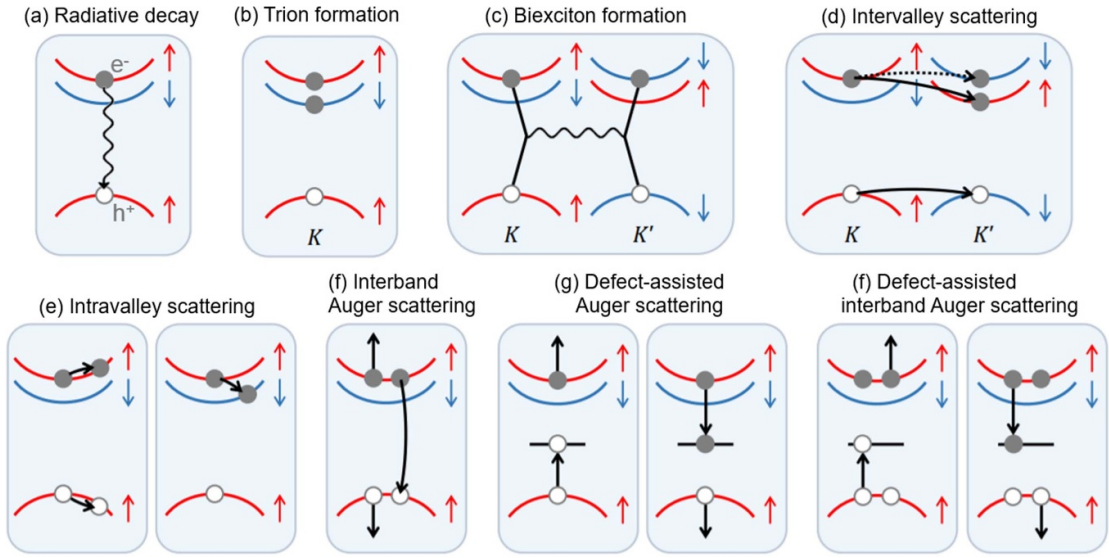

Figure 2. Radiative and non-radiative recombination pathways in monolayer TMDCs. Here, exciton, trion and biexciton decays can all be radiative and are associated with their own spectral characteristics. The other processes are scattering processes that change occupations of excitonic states, which might be monitored under the right experimental conditions with transient absorption spectroscopy, for example. Reproduced with permission from [62].

are combined into HSs. For example, the valley polarization, which is lifted in monolayers due to the electron–hole exchange interaction, can be more protected in HSs due to small wavefunction overlap for the IE [73–75]. Before using these sophisticated effects in applications, however, much work remains to be done to elucidate the structure–property relations of HSs. In the following sections, we briefly touch on the very rich field of TMDC–TMDC HSs before going more deeply into recent results of mixed HSs.

3. Heterostructures

2D TMDC monolayers can be stacked on top of each other, bound by Van der Waals interactions to form either homostructures—where the layers are composed of the same material, or HSs—where the TMDC monolayers are made up of different materials [76, 77]. The HSs can be fabricated using a variety of techniques, the most common of which include mechanical exfoliation by either a wet or dry transfer process, followed by contact transfer and chemical vapour deposition (CVD). Microscope images of HSs fabricated by mechanical exfoliation are shown in figure 3 [28, 78]. As the HSs are bound by Van der Waals forces and do not involve atom-specific bonding, there is a myriad of possible combinations of Van der Waals HSs. For this reason, interest in HSs has been continuously rising over the past years. Between 2012 and 2022, for example, there have been on average 860 additional works published compared to the previous year [79]. These works include the fabrication of 2D TMDC/TMDC HSs, along with 2D TMDCs that are stacked with entirely different materials into HSs, such as 2D perovskite microplates and 0D perovskite quantum dots (QDs), as we will discuss later.

The potential for stacking different materials, without a strong necessity of lattice matching, promises highly tunable HSs with properties that can be vastly different from any of the constituents. An important ingredient in understanding HSs is their band alignment, which results from the respective energies of the electronic bands of the two materials, and determines whether charge or energy transfer occurs between them, as discussed below. Furthermore, some HS properties result from the formation of defect states, which can lead to substrate effects on interlayer interactions, for example [81–83]. Finally, an intriguing aspect of HSs is the formation of IEs, formed as a result of charge transfer across the two materials. These IEs differ significantly from excitons in single monolayers, as the constituent charges of IEs are separated, located in the opposing layers. Furthermore, besides having the freedom of stacking different compounds, it turns out that the angle under which the two, or more, layers are stacked affects the optoelectronic properties of the HSs to a great degree. These stacking-angle dependent systems are called Moiré HSs, and they will be discussed in more detail below. In any case, due to the specific band alignments, the stacked HS can be thought of as an entirely new material compared to the individual constituents and hence opens an entirely new field in optoelectronics.

3.1. Band alignments

The relative energy levels of the electronic bands of the stacked materials give rise to characteristic band alignment, which determines much of the properties

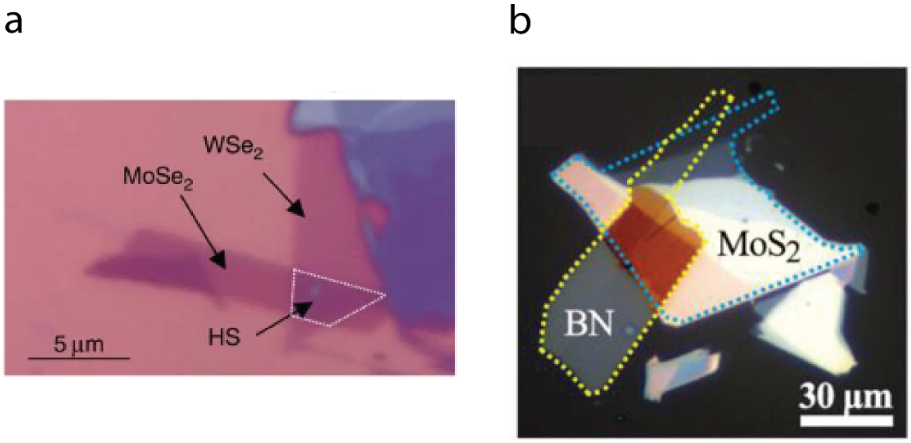

Figure 3. Optical microscope images of two heterostructures. Both heterostructures were fabricated using mechanical exfoliation of the individual materials and subsequent stamping. (a) A heterostructure of the two semiconductors $MoSe_2$ and WSe_2. Reproduced from [14], with permission from Springer Nature. (b) A heterostructure of MoS_2 and the insulator hBN, [80] John Wiley & Sons. © 2019 WILEY-VCH Verlag GmbH & Co. KGaA, Weinheim.

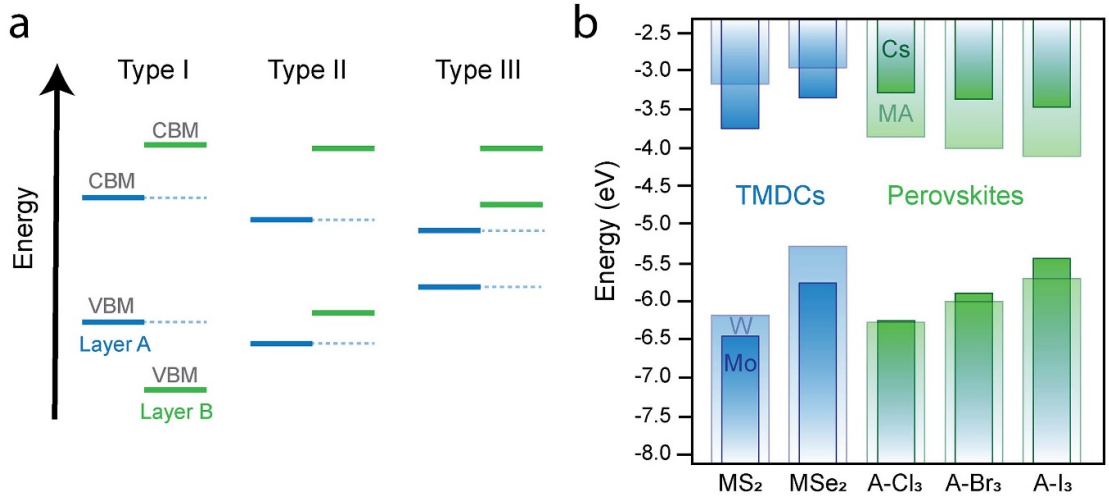

Figure 4. (a) The three types of heterostructures. Solid lines indicate the energies of bands for material A (blue) and material B (green), with dashed lines added merely as a guide to the eye. Depending on the relative energies of the bands, type I, II and III can be distinguished. (b) Band energies of common TMDCs (blue) and lead-based perovskite materials (green). The band energies of the TMDCs are calculated using the G_0W_0 method [87], with solid boxes indicating molybdenum compounds and transparent boxes indicating tungsten compounds. The perovskite materials have the chemical formula $APbX_3$, where solid boxes show perovskites with the A = Cs cation [88], and transparent boxes show band energies with A = methyl ammonium (MA) compound [89], and X is a halide (Cl, Br, I) as indicated.

of the HS. One can distinguish three types of alignments, as summarised in figure 4(a): in a type I alignment, the valence band maximum (VBM) and conduction band minimum (CBM) of material A are sandwiched by the valence and conduction band extrema of material B. In this case, both electrons and holes tend to diffuse into the material with the smaller bandgap, and thus energy transfer can occur from material B to A. In a type II alignment, the bands are staggered, meaning that both the VBM and the CBM of one material lie above those of the other material. This favours charge separation at the interface of the two materials, where electrons and holes experience opposite driving forces, and thus get transferred into opposite layers. This alignment is the one required for photodiodes or solar cells to separate photo-generated charges. A rare case is the type III HS where the energies of both valence and conduction band extrema of one material lie above the CBM of the other, creating a so-called broken gap. Because electrons and holes now experience a large potential barrier at the interface, charge transport is essentially only possible due to tunnelling, and thus this type of band alignment can be used to create tunnelling junctions [84–86].

The band alignment is generally calculated by density functional theory (DFT) or by the single-shot perturbative G_0W_0 approximation to determine the work functions [87]. The G_0W_0 is also referred to as the dynamically screened interaction;

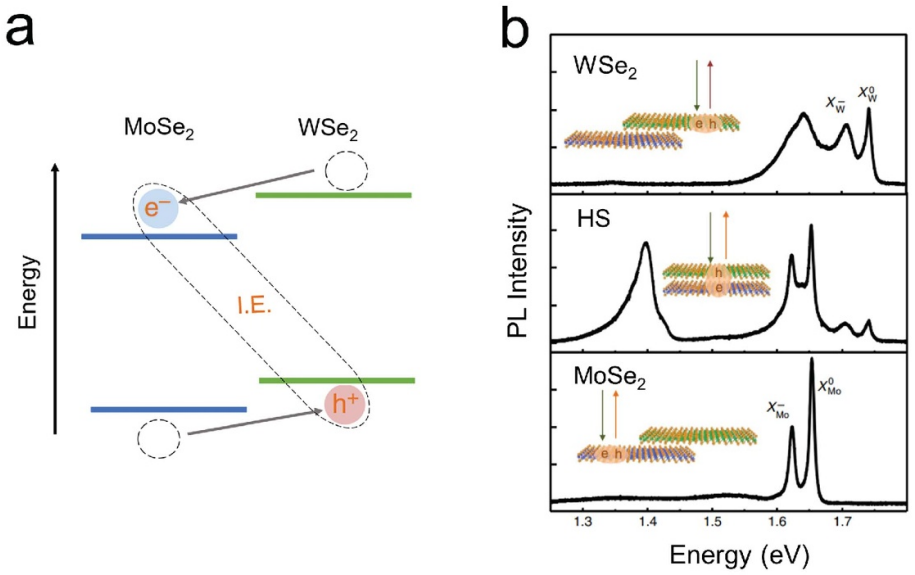

Figure 5. (a) Band alignment and formation of an interlayer exciton in a $MoSe_2/WSe_2$ heterostructure. (b) Photoluminescence spectra , taken at 20 K, of the WSe_2 and $MoSe_2$ monolayers and their heterobilayer. The peak at 1.35 eV was attributed to the interlayer exciton emission. Reproduced from [14], with permission from Springer Nature.

in this approximation, the multi-body electron–electron interactions are captured in a quantity called the electron self-energy and are calculated as a product of Green's function (G) with the screened interaction (W) [90–92].

Experimental methods such as microbeam scanning tunnelling microscopy (STM), high-resolution x-ray photoelectron spectroscopy (XPS), ultraviolet-visible (UV–VIS) spectroscopy and angle-resolved photoemission spectroscopy can then be used to extract the valence band and conduction band offsets and the electronic band gap of the material [93–95].

From the obtained energy values, the band alignment of the HS can be determined [96, 97]. Figure 4(b) shows an overview of band energies for the most common TMDCs, calculated using the G_0W_0 method [87], and PMs, obtained through experimental [88], and DFT techniques [89].

3.2. Interlayer excitons in TMDC/TMDC heterostructures

TMDC HSs were first reported by Fang and co-workers in 2014, who fabricated a WSe_2/MoS_2 structure [13] by mechanical exfoliation and subsequent stacking of the exfoliated monolayers on top of each other. This technique is now common throughout the literature and allows for convenient identification of the separate monolayers, and the HS region where they overlap, using techniques like room-temperature optical microscopy, Raman spectroscopy, TEM and photoemission electron microscopy. With absorption measurements, the authors showed that the HS region exhibited an absorption profile that is roughly a linear combination of the individual monolayers. Contrastingly, the PL measurements showed quenching of the main exciton peaks of both materials and an additional lower-energy peak. These results suggested that the extra PL peak is not due to a shift of the main exciton lines, but rather due to the HS. The authors attributed this peak to the relaxation of electron–hole pairs bound across the interface; they showed that the PL signal of this feature decreases as hexagonal boron nitride (hBN) layers are introduced between the WSe_2 and MoS_2 layers, supporting the idea that this PL feature originates from interface-separated bound charges. The interfacial electron–hole pairs from this interpretation came to be called IEs and result from HSs of a type II alignment. Subsequent work on a $MoSe_2/WSe_2$ HS similarly identified a lower-lying PL peak, see figure 5, and found that this state is long-lived, with a lifetime of 1.8 ns [14], much longer than the typical PL lifetimes of excitons and trions, which are on the order of 10 ps for TMDC monolayers [98]. Such slow radiative recombination has also been observed in $MoS_2/MoSe_2$ HSs [99], indicating that the increased average lifetime measured for TMDC/TMDC HSs is a general property of IEs in group-VI TMDCs. Since then, similar PL signatures have been observed in several other works [100–103], and the measurements were expanded to temperature-dependent PL [102]. In addition, electrostatic gating was introduced to tune the energy of the IE, as shown in figure 6. The vertically separated charges across the stacked layers are associated with an electric dipole moment along the out-of-plane direction, which can be modulated by an

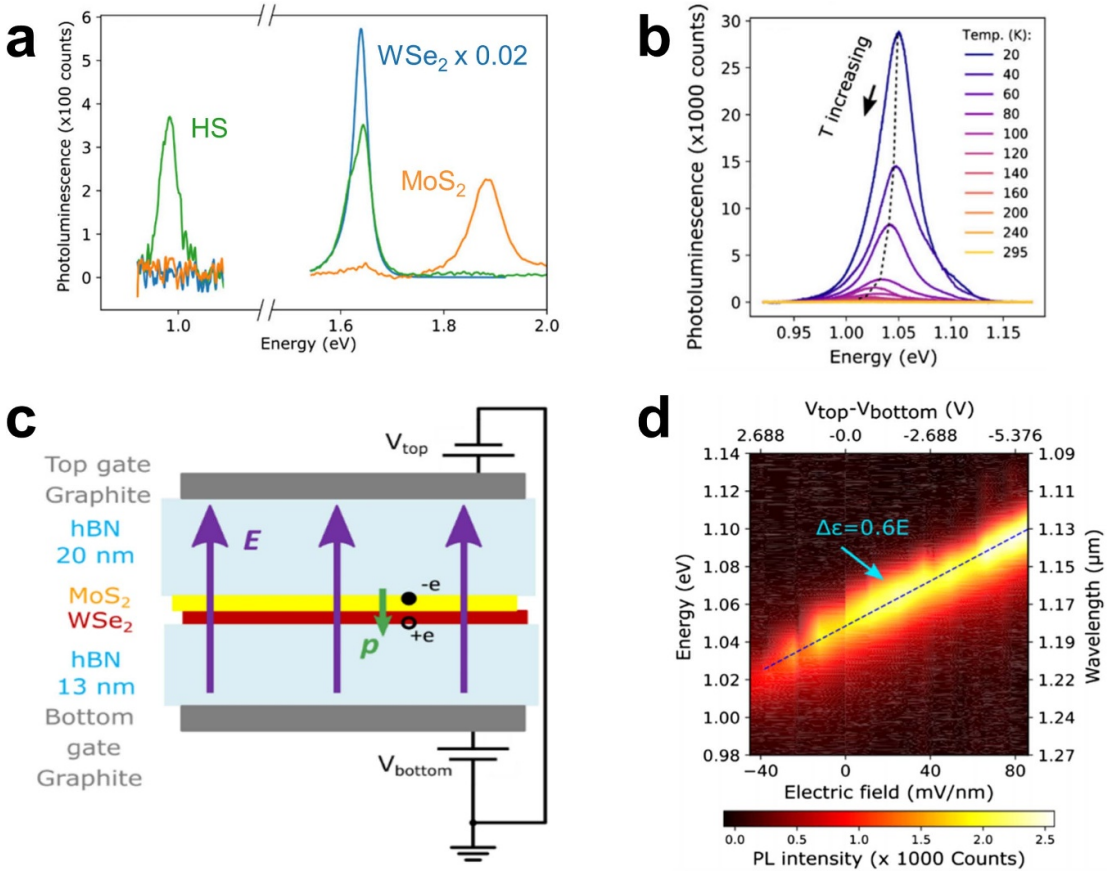

Figure 6. (a) PL spectra indicating the formation of interlayer exciton in a MoS_2/WSe_2 based on the quenching of the intralayer exciton emission. (b) Variation in the PL emission band of the interlayer exciton in the same HS as a function of temperature. (c) A gated device was fabricated in order to apply an out-of-plane electric field to the HS. (d) PL spectra of the interlayer exciton as a function of the applied voltage to the gated device. Reprinted with permission from [102], Copyright (2019) by the American Physical Society.

electric field induced by an electrostatic gate. Such a static dipole moment is not expected from defect states, thus the observation of electrical modulation of the PL feature provides important support to the existence of IEs [102].

Crucial theoretical insight came from studies on a MoS_2/WSe_2 HS, where PL spectroscopy was combined with DFT calculations to show that the lower-energy IE feature in the PL spectra could be explained by a $\Gamma \rightarrow K$ transition, showing that the exciton is not just characterized by a lower spatial overlap of the charges due to the layer separation, but its recombination also involves a momentum-indirect transition [104]. Similarly, another study attributed spectroscopic features of TMDC HSs to momentum-indirect transitions [105], although a $MoSe_2/WSe_2$ HS was suggested to have interlayer features comprised of both direct and indirect transitions [106]. Such momentum-indirect transitions are consistent with the direct-to-indirect transition in bilayer homostructures as the orbital character of TMDCs at the Γ and Λ points have significant out-of-plane character [32–34]. These points in the electronic bandstructures of the HSs are sensitive to both interlayer distance and interlayer stacking angles and can thus be altered by stacking. These features support the observations of predominantly momentum-indirect IEs and are consistent with their long PL lifetimes [74].

Detailed studies on the formation and decay kinetics of excitons in TMDC/TMDC HSs were first performed by Hong and co-workers [107]. They used pump-probe spectroscopy on the femtosecond time scale along with PL measurements to study the ultrafast dynamics of charge transfer across the interface, inspired by previous studies, which demonstrated ultra-fast charge transfer kinetics in organic heterostructures that were also bound together by Van der Waals forces [108, 109]. Hong's work focused on MoS_2/WS_2 layers that exhibit a type II band alignment. Low-temperature (77 K) and room-temperature PL measurements showed strong emission intensities in the separated monolayers, but PL quenching in the combined HS, indicating possible charge transfer. When resonantly pumping at the energy of the MoS_2 A exciton and probing the absorption of the HS, the authors found a pump-induced decrease of absorption in both materials, even though the A and B exciton lines of WS_2 had energies far above the pump energy. This pump-induced decrease

of absorption is indicative of charge transfer since the generated charge carriers after transfer occupy states which reduce the absorption. Confirming that the TA signal resurges in isolated WS_2 then consolidated the interpretation of charge transfer from MoS_2 to WS_2. Additionally, by varying the delay time of the probe, the authors determined that holes from the MoS_2 layer had migrated into the WS_2 layer within 50 fs after irradiation by the pump. These kinetics were observed both at 77 K and at room temperature. Other works, such as that of Ceballos and co-workers, yielded similar results for a $MoS_2/MoSe_2$ heterobilayer [110]. These examples indicate how optical methods can provide insight into charge transfer processes in the TMDC/TMDC heterobilayers [107, 110, 111].

IEs typically recombine at a much slower rate than intralayer excitons as a result of the reduction in the spatial overlap of their wavefunctions [112–114]. The average IE lifetime spans from the order of 50 ps to 1.5 ns, depending on the stacking nature of the layers and the nature of exciton recombination [115]. Hence, recombination lifetimes can be prolonged not only by varying the stacking order but also by measuring at lower temperatures, measuring with a different twist angle, increasing spatial separation of the monolayers and synthesising the HS with a different technique [116, 117]. Furthermore, differences in the photoluminescence spectra and kinetics between TMDC HSs and their monolayers can also be ascribed to surface defect states and other radiative trap states [63, 113, 118–120]. Therefore, single-experiment characterisation, using PL or TRPL alone, is generally insufficient to conclude on the formation of IEs. An additional powerful technique is cathodoluminescence (CL), in which electrons are used to locally excite charge carriers to obtain insight into their local radiative decays, achieving superior spatial resolution in photoemission mapping. While this technique has been applied to IEs to identify and isolate them from intralayer excitons [121, 122], comprehensive work including both steady-state and time-resolved CL is limited, but could provide further insights on the nature of IEs.

3.3. Moiré excitons

One of the critical tuning parameters in stacked TMDC HSs is the relative angle of orientation between two layers. This twisting angle plays a pivotal role in shaping the electronic properties of the resulting structure. For example, in bilayer graphene, the stacked material undergoes a transformative shift into a superconducting state at a highly specific twisting angle, commonly termed the 'magic angle' [123]. The intricate electronic effects induced by the twisting angle create a Moiré pattern—a superlattice formed by the periodic interference between the two layers. Under a specific stacking angle, this leads to the emergence of a flat electronic band, intensifying electron correlations and facilitating superconductivity in the specific case of bilayer graphene [124, 125]. In TMDC HSs, several works have explored the effects of variable stacking orientation and twisted layers. This exploration has revealed a new class of quasiparticles known as Moiré excitons [126–128]. The Moiré excitons can be interlayer or intralayer in nature. These twist-induced excitonic states exhibit enhanced binding energies and, provided that the Bohr radius of the Moiré exciton is smaller than the Moiré pattern itself, long-range spatial periodicity—properties which are distinct from excitons found in individual TMDC layers [129]. In addition to their formation, the precise behaviour of the Moiré excitons is significantly affected by the difference in the twist angle between the TMDC bilayers [130, 131]. For example, with an increasing twist, regions of constructive interference in the Moiré pattern become more localised, which in turn affects the spatial distribution of the excitons themselves. Furthermore, changes in the electronic band structure due to variations in the Moiré pattern will directly impact the absorption and emission characteristics of the Moiré excitons—an increase in twist angle will lead to shifts in the optical signatures associated with Moiré excitons [132, 133].

We note that PL and TRPL are not the only optical techniques applied to study the precise properties of IEs. Reflection spectroscopy has been used as an additional assessment tool to provide further insight into the excitonic nature. As an example, optical spectra, measured at 10 K, were employed to study the twist-angle dependent properties of the IE in the WSe_2/WS_2 TMDC HS under different angles of orientation, after the presence of an IE peak was established from PL [126]. The authors showed that a near-zero twist angle contributes to a much stronger enhancement of the interlayer excitonic peak than a larger angle. This is attributed to the Moiré pattern at the near-zero twist angle generating distinct Moiré exciton states, which are then visible in the reflectance spectra. Notably, the reflectance spectra were directly compared to the PL excitation (PLE) spectra, and found to yield the same excitonic features. With properties such as the ones discussed above, Moiré excitons in TMDC heterobilayers have expansive potential applications in the fields of 'twistronics' (utilising the twist-dependent electronic properties of the system), nano-photonics and quantum information [134, 135].

3.4. Janus layers

Over the past few years, alloying has emerged as a powerful technique to tune the structure and optoelectronic properties of TMDCs. In this fabrication technique, layers of $M_yM'_{1-y}X_2$ or $MX_{2y}X'_{2(1-y)}$ are synthesised by varying the composition (y) of the metal (M/M') or chalcogen (X/X') atoms [136–138].

By controlling the alloying composition in each individual layer, fundamental properties such as bandgap and effective mass can be effectively modified [136, 139, 140]. Both theoretical and experimental studies have shown composition-dependent bandgaps in the TMDC alloys and the obtained results have opened possibilities of bandgap engineering [136, 141–143]. Since the alloyed layers can be used for stacking, this further expands the space of HS possibilities for the TMDCs.

Interesting examples of alloyed layers are Janus monolayers, where the controlled mixing of chalcogen atoms leads to bottom and top chalcogen planes of different composition. This results in an out-of-plane dipole, as for the layered HSs [144]. However, due to the complete absence of any real stacking, there is no possibility of momentum mismatch, and the optical transitions tend to be at energies in between those of the pure compounds [145]. One study fabricated WSSe/MoSSe and WSe_2/WSSe HSs by a combination of plasma-induced vacancy formation coupled with a CVD process [145]. The PL spectra of the HSs clearly showed that the HSs exhibit PL from both layers, yet no clear conclusions were drawn on charge transfer effects. Another study on stacking Janus monolayers investigated the effects of the built-in field from the different chalcogen planes on charge transfer rates in a WSSe/WS_2 HS and found that the Janus-induced electric field can function as an additional potential barrier, prohibiting charge transfer, even when the type II band alignment suggests its possibility [146]. This makes the charge transfer rate directional and dependent on the stacking sequence. A further alloying possibility is the alloying of the metallic component, followed by HS formation, creating layers with different metallic constituents. This has been explored briefly in early work where HS alloys were directly grown by CVD [147]. While the HS composition was indeed verified through Raman and PL techniques, however, no clear analyses were performed on charge transfer, leaving it as an interesting future research direction. These examples show that, already within the TMDC family, there is a lot of design space for fabricating HSs with diverse functionality. This design space can be further expanded by stacking TMDC monolayers with completely different compounds. This direction will be discussed in the following section, focusing on TMDC/perovskite HSs.

4. TMDC-perovskite heterostructures

The performance of 2D TMDC/TMDC HSs in optoelectronic devices is limited by low light absorption, related to their single atomic layers, which is particularly undesirable for photovoltaic applications. One way to improve the overall absorbance is to replace one of the TMDC layers with a strongly absorbing material. This strategy has been demonstrated for organic materials, carbon nanotubes and QDs [148–152]. As the potential number of candidate materials for forming HSs with TMDCs is huge, in this review we focus specifically on HSs of TMDCs with halide PMs. Perovskites can effectively enhance absorbance, even though the absorption coefficient of a monolayer of a typical perovskite is roughly the same as that of a TMDC monolayer [153]: nevertheless, as their carrier transport is very efficient, thick perovskite layers can be used for the absorption, absorbing sufficient amount of light to create charge carriers, which can then migrate to the HS interface. In the following, we will first review the most basic properties of perovskite structures, before we go into more detail about perovskite/TMDC HSs.

4.1. Perovskite

We will primarily focus on HSs consisting of the conventional perovskite with the ABX_3 crystal structure, wherein A corresponds to a small cation, such as Cs^+ or methylammonium (MA^+), B corresponds to a large cation, such as Pb^{2+} and Sn^{2+}, and X is a halide anion or some mix of halide anions. Much has been written on the chemical and optoelectronic properties of these perovskites and we refer the reader to some in-depth reviews [154–158]. Briefly, semiconducting inorganic $CsPbX_3$ materials, where X is a halide atom, have been known to crystallise in the perovskite structure since the 1950s, [159], and the prototypical organic–inorganic compound of methyl-ammonium lead halide ($MAPbX_3$) was subsequently described in the 1970s [160]. Differences in A-site cations (MA versus Cs) not only result in structural differences and relative differences in stability ($CsPbBr_3$, which is the more stable of the two, is typically found in the orthorhombic phase at room temperature, while $MAPbBr_3$ is found in the cubic phase) but also results in optical and optoelectronic changes in the material—for example, the band gap of $MAPbBr_3$ tends to be lower than $CsPbBr_3$ [161, 162]. Going from bulk to confined systems, the 2D-layered, Pb-based, perovskites were first synthesised in the 1980s [163], and basic optical properties were described in the early 1990s [164]. The main motivation for studying these layered crystals was that they act as natural quantum well systems, due to the Van der Waals interactions between the layers, as opposed to the heavily designed GaAs-based wells. Subsequently, perovskites experienced a resurgence as high-efficiency emitters due to the landmark paper by Kovalenko's group on the synthesis of $CsPbX_3$ nanocrystals in 2015 [165]. Clearly, TMDCs and PMs overlap in the motivation for studying systems with strong excitonic behaviour, and it is no surprise that after these low-dimensional systems were shown to be stable in practice, the field quickly moved to combine these two classes of semiconductors.

What makes the PMs interesting candidates for HSs with TMDCs, is, next to their bandgap tunability by composition, the fact that carrier transport in the perovskites has been shown to be effective enough for the migration of charges to the HS interface even if the perovskite layer is 200 nm thick [166, 167]. This might be in part due to a process called photon recycling in PM that effectively enhances carrier diffusion lengths by repeated absorption and emission events [168]. The thickness of these perovskite layers can be increased without significantly changing the electronic bandstructure, while for TMDCs clear changes in bandstructure and excitonic properties occur with increased thickness. Therefore, the addition of a perovskite layer might enhance flexibility and tunability in HS properties without sacrificing potentially desired TMDC monolayer properties. In the following, we discuss multiple dimensionalities of perovskites, from bulk to nanocrystals. This is an important distinction as nanocrystals, for example, are typically capped with stabilising ligands [165], which can potentially affect the HS interface. Thus, we will specify the perovskite dimensionality for each discussed work.

4.2. Band alignment engineering

The first reports of TMDC/PM HSs date from 2016, where $MAPbI_3$ thin films (10s–100s nm thick) were used as the perovskite layer [169–172]. While MoS_2 had been used before as a hole-transport layer in organic solar cells, [173], in the TMDC/perovskite HS, it was used for the first time as an active absorbing layer, next to the perovskite layer. To tune the charge and energy transfer between the perovskite and TMDC, modulation of the band alignment between these two materials is essential. In this context, the work by Peng and co-workers is particularly interesting, who analysed charge transfer processes in a $MoS_2/MAPbI_3$ perovskite HS, where the $MAPbI_3$ was 30 nm thick [171]. They experimentally analysed the excitonic states using pump-probe spectroscopy in a similar manner to what has been described in section 3.2. The work reported that the band edge alignment can be tuned by defect engineering: the type I heterojunction could be converted to a type II heterojunction using oxygen plasma treatment of MoS_2. As a result of the band-alignment engineering, competitive charge transfer and energy transfer mechanisms could be varied. This work demonstrated highly efficient charge transfer in which 83% of the holes generated in the perovskite were transferred to the MoS_2, on a timescale of 300 fs after photoexcitation. The fact that defects can play a strong role in the performance of these mixed HSs was explicitly investigated in another work, in which defects were passivated in a CVD-grown WSe_2 monolayer through laser-induced oxidation. The photo-responsitivities of the resulting HS with a bulk-like film of $MAPbI_3$ device with the treated monolayer were higher than the device with the untreated monolayer [172]. The more diverse band alignments in these mixed HSs are a main advantage over the typical TMDC/TMDC HSs, which generally form type II band alignments, as shown in figure 4. However, as the previous works show, the role of TMDC defects can not be neglected in the characterisation of the HSs.

In the following years, more works on the device performance of these HSs were published (see [176–181], for a selection, with various perovskite compositions and morphologies). While most of these works rely on the electronic charge- or energy transfer, it is worth pointing out at least one study that used the excellent emissive properties of a 37 nm thick layer of $CsPbBr_3$ nanocrystals and subsequent radiative energy transfer to effectively boost the absorption of the underlying MoS_2 layers [182]. Other works also went more deeply into the processes underlying the energy and charge transfer in the HSs. In this regard, the work from Bauer *et al* focused on a 100 nm thick film of $MAPbI_3$ perovskites but with WS_2 as the TMDC in the HS [174]. Akin to TMDC/TMDC HS analysis, they used microscopic ultra-fast pump-probe transient spectroscopy measurements combined with room-temperature PL spectroscopy, to determine the kinetics within the HS. This work presented a somewhat unusual finding: despite a type I band alignment, for which energy transfer and hence PL emission would be expected (figure 7(a)), the PL contributions from the individual constituents were quenched (figure 7(b)). As the PL was quenched in both materials, the authors concluded that energy transfer was not the dominant transfer mechanism. Rather, the strong binding energy of the excitons in the TMDCs and the small energy difference between the VBMs of the two materials limited the transfer of holes to the perovskites. While the holes from the B-exciton band could still transfer, the effective hole transfer rate was smaller than the electron transfer rate, for which both A-exciton band and B-exciton band electrons could contribute in the transfer from the TMDC to the perovskite. This resulted in an HS dominated by charge, not energy, transfer. This suggests that the peculiar spin–orbit physics of TMDCs has far-reaching effects for their functionality in HSs, opening up sophisticated ways of manipulating charge transfer by comparing A-exciton and B-exciton dissociation rates.

Extending these band alignment considerations further, a HS of monolayer MoS_2 and 40 nm thick $CsPbBr_3$ nanosheets, with a type II alignment was reported [176], while another work showed a type I alignment between $CsPbBr_3$ nanowires and monolayer MoS_2 [183]. Similarly, a WS_2 monolayer/$CsPbBr_3$ 180 nm thick microplate HS exhibited a type II alignment in one study [101], while

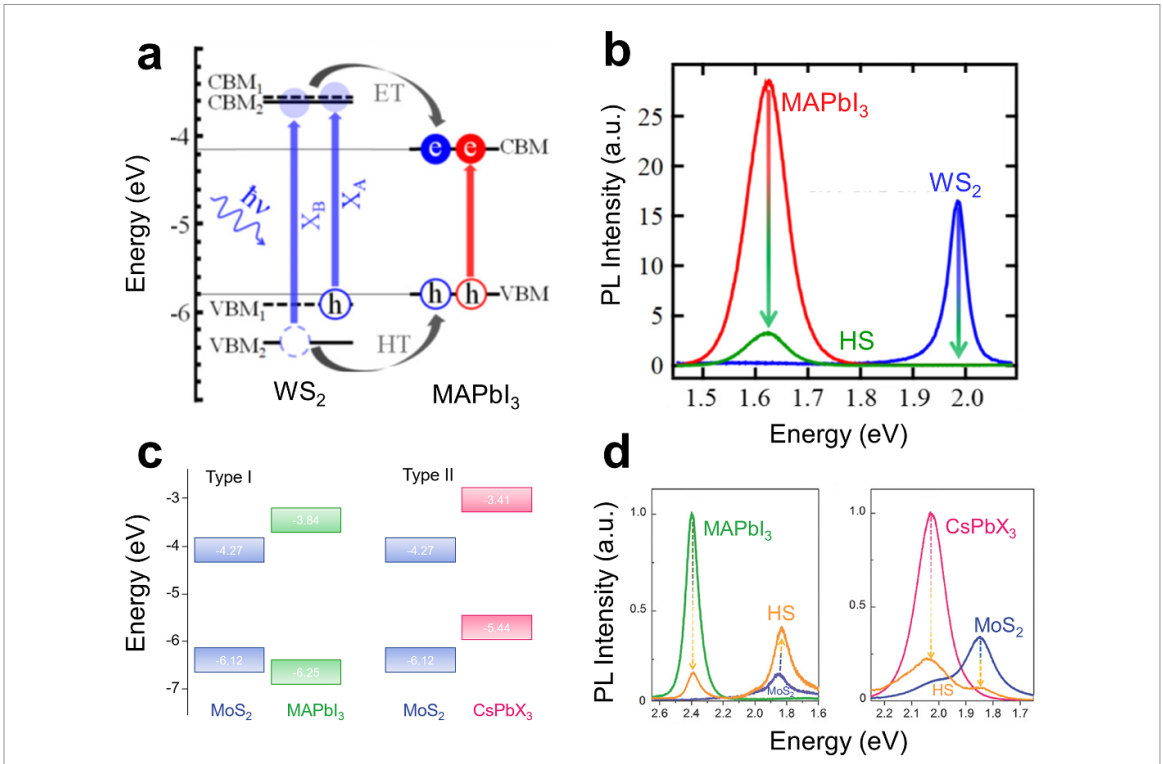

Figure 7. (a) Type I band alignment of a $MAPbI_3/MoS_2$ HS, $MAPbI_3$ nanocrystals had an average diameter of 7. (b) Room-temperature PL spectra of the pristine layers and the HS of $MAPbI_3/MoS_2$. Despite a type I system, the PL quenching from the constituent emission bands suggests charge transfer occurs in this system. (a), (b) Reprinted with permission from [174]. Copyright (2018) American Chemical Society. (c) Band alignments of the compared structures in Wu's study, where the $CsPbX_3$ had an average diameter of 15 nm. (d) The compared samples' pristine and HS room-temperature PL spectra. (c), (d) [175] John Wiley & Sons. © 2018 WILEY-VCH Verlag GmbH & Co. KGaA, Weinheim.

in another study, WS_2 with $CsPbBr_3$ QDs (average size of 11 nm)—rather than sheets—resulted in a type I alignment [184]. In both examples, the calculated or measured bandgaps of the PMs did not change significantly; rather, the morphology and dimensionality of the perovskites seem to have caused the shift in band alignments. In terms of material dimensions, it was shown that the diffusion length of charges in a $CsPbBr_3$ film is sufficiently long that perovskite films from 8 nm up to 200 nm thick can still efficiently transfer charges to TMDC monolayers [166, 167]. These examples indicate that the relative ease of solution processing of the perovskites combined with the spin–orbit split bands in the TMDCs allows a wide variety of band alignments to be engineered. As pointed out before, these spin–orbit split bands cause alignments that are neither precisely type I nor type II but create competing transfer processes [184].

Naturally, adjusting the perovskite bandgap by composition is a powerful way of tuning band-alignments. In 2018, a comparative study on the differences in the band alignments for inorganic and organic perovskite QDs, namely $MAPbBr_3$ and $CsPbBr_{3-x}I_x$, with average diameters of 7 nm and 15 nm respectively, in MoS_2 HSs was published [175]. Using ultra-violet photoelectron spectroscopy measurements, the work showed that organic $MAPbBr_3/MoS_2$ heterobilayers formed a type I band structure, while the inorganic $CsPbBr_{3-x}I_x/MoS_2$ HS formed a type II structure (figure 7(c)). In line with the general PL quenching trend in type II structures, the $CsPbBr_{3-x}I_x/MoS_2$ showed PL quenching in both layers, while for the type I HS, the PL intensity was quenched only for the $MAPbBr_3$ QDs, but enhanced for the MoS_2, highlighting the role of band alignment in the excitonic charge and energy transfer. The PL spectra obtained from this study are shown in figure 7(d). In addition to the PL and TRPL analyses, the authors also studied the optoelectronic performance of these HSs by separately incorporating them into photofield-effect transistors (PFETs). In both devices, the HSs were fabricated on top of back-gate SiO_2/p-type Si substrates, and Au/Cr contacts were evaporated onto the substrates as the source and drain contacts. The performance of each system was analysed by current–voltage sweeps in the dark and under illumination. The measured photocurrent of the all-inorganic type II HS was more than four times that of the organic–inorganic type I HS. The superior optoelectronic properties of the all-inorganic HS was attributed to trapped long-lifetime carriers in the surface states or interface trap states, particularly arising from the MoS_2 interface. The Cs-based system's ability to transfer photoexcited electrons while accumulating photogenerated holes resulted in a strong photogating effect, contributing

to the overall enhanced optoelectronic performance. Conversely, both of the photogenerated electrons and holes were transferred to the MoS_2 layer in the MA-based system, where they subsequently recombined; this ultimately led to a relatively poor performance in the organic–inorganic device. More generally, the authors argue in this work that the advantageous optoelectronic properties coupled with the higher overall stability of $CsPbBr_3$ perovskite QDs may lead to more favourable TMDC/perovskite HS systems and devices in the future.

As shown by the Kovalenko group, the bandgaps of the all-inorganic perovskite nanocrystals change with the halide element, from around 3 eV in $CsPbCl_3$ via 2.4 eV for $CsPbBr_3$ to 1.8 eV for $CsPbI_3$ [165]. This change in bandgaps is accompanied by a change in band energies [88], and it will be interesting to see if the facile change in halides can induce a change from a type II to a type I HS. However, no systematic experimental study exists yet on this halide-dependent band alignment in an HS with TMDCs. Clearly, the facile exchange of cations and anions in semiconducting PMs promises a wealth of tunability for HSs in the near future.

Finally, further opportunities for interfacial engineering in TMDCs/perovskite HSs arise through the surface chemistry of the perovskites, or by inserting spacer layers between the two materials. Using room-temperature, TRPL spectroscopy, Liu *et al* showed that the introduction of hBN spacer layers between all-inorganic perovskite nanocrystals, with average sizes of 8.5 nm and monolayer MoS_2 altered the PL lifetime of the perovskite nanocrystals, with shorter lifetimes for thinner spacers [80]. They showed that the charge transfer rates can be effectively modulated by introducing hBN flakes of up to 7 nm thick. Using ligand engineering in the same HS, albeit with slightly larger nanocrystals of around 15 nm, interfacial charge transfer was enhanced by removing as much of the nanocrystal ligands as possible without compromising the stability of the perovskite nanocrystals [185]. With this treatment they improved the photo-responsitivity of their photodetector devices by a factor of 15. Another approach to ligand engineering exists for quantum-confined nanocrystals, where the choice of surface ligands can affect the band alignments, without changing the bandgap. This has been shown before for QD HSs [186], but to our knowledge, not yet for mixed TMDC–perovskite HSs.

The above examples demonstrate that elemental composition, dimensionality, morphology, defects, layer distances and surface chemistries of a TMDC/perovskite HS can all alter the band alignment of the HS, which in turn, determines the extent of charge or energy transfer between the layers. As a consequence, the simple band alignment picture is not always indicative of charge or energy transfer

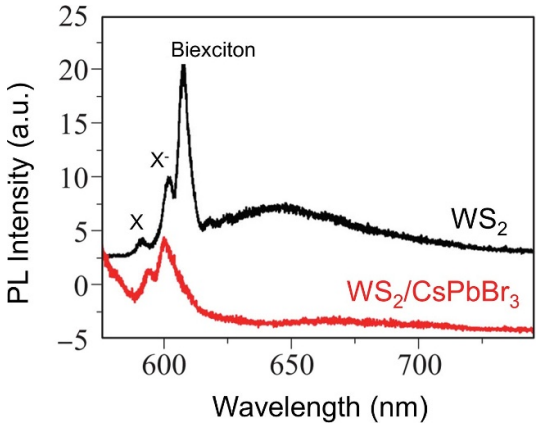

Figure 8. Low-temperature PL spectra of the WS_2 pristine sample and the $WS_2/CsPbBr_3$ HS. The $CsPbBr_3$ consists of 180 nm thick microplates. Note the emission differences from the neutral exciton (X), the charged exciton (X^-) and the biexciton between the spectra. Reproduced from [101], with permission from Springer Nature.

processes, as can be seen by comparing the panels of figure 7. Rather, a combination of experimental methods such as (time-resolved) PL and TA spectroscopy is required to determine the charge kinetics in TMDC/perovskite HSs.

Therefore, the same combination of techniques that already provided insight into the charge dynamics of TMDC/TMDC HSs is useful in elucidating the carrier dynamics in the TMDC/perovskite HSs, as will be discussed in the following sections.

4.3. Signatures of charge transfer

Steady-state PL spectroscopy, particularly PL spectroscopy at low temperatures, is a convenient technique to optically characterise the TMDC/perovskite HSs. In Wu's comparative analysis, the PL quenching in the $CsPbX_3/MoS_2$ HS indicated full energy transfer, while the PL quenching of the organic perovskite along with the PL enhancement of MoS_2 indicated charge transfer [175]. This argument is generally applied in most TMDC/perovskite reports [101, 184, 187].

Besides that, low-temperature PL measurements can provide insights into the kinetics of the biexcitons and charged excitons within a TMDC/perovskite HS, which otherwise would not be observed. For example, one study reported the PL of a WS_2/microplate $CsPbBr_3$ structure and its pristine components at 3.3 K to resolve the excitonic emission bands [101]. As the density of the biexcitons varies quadratically with the number of excitons in the pristine TMDC monolayer, small fluctuations in the exciton density, which may be undetectable in many PL systems, can be detected from changes in the biexciton emission (figure 8). Additionally, since the binding energies of trions and biexcitons are lower than those of neutral excitons, the driving force for charge separation at the

interface will be more effective for these exciton complexes. At low temperatures, the authors observed full quenching of the biexciton emission in the HS compared to the monolayer, indicating that charge transfer occurred within the sample.

Adhikari *et al* further studied the excitonic room-temperature PL spectra of a CVD-grown monolayer MoS_2 and 11 nm sized $CsPbBr_3$ nanocrystals HS and noted that each of the neutral A and B excitons and the negatively charged A^- exciton red-shifted in the HS [188]. Their argument was further strengthened by showing more dominant trion emission, independent of laser power, and related shifts and power dependence in TA measurements. Furthermore, by constructing gated devices with and without the QDs, the work also found a downshift in the threshold voltage in the HS compared to the pristine device. Both indicate that the MoS_2 layer's electron concentration was higher in the hybrid than in the pristine sample. In turn, this implied charge transfer had occurred in the HS, with electrons transferred from the QDs to the MoS_2. Overall, this study highlights the difficulty of characterising charge transfer by exciton lines, as both the exciton binding energy as well as the electronic bandgap can shift with the influx of charges.

Before we continue towards alternative signatures of energy transfer, we briefly exemplify a lead-free system, namely the evaporated $CsSnBr_3/WS_2$ (grown by CVD) HS as recently fabricated and characterised in the work of Mu *et al* [189] The key novel concepts summarised from this work are two-fold: first, as it has been argued that toxicity of lead will limit the extent of future applications for any perovskite optoelectronic device, a substitution of lead by another element such as tin is necessary. Second, contrary to the majority of published works using mostly solution-processed methods such as mechanical exfoliation or vacuum deposition to prepare the perovskite, in this study, precise tuning of the perovskite thickness (varying between 10 nm and 70 nm) was achieved using thermal evaporation. The optical properties were characterised using UV–VIS absorption spectroscopy, steady-state PL and TRPL. Using UV–VIS measurements supplemented with XPS, the HS was found to exhibit type-II band alignment. The observed PL quenching in this system together with the differences in TRPL lifetime was attributed to charge carrier transfer across the system. This work by Guo *et al* is a pioneer study on the use of lead-free perovskites in TMDC-based HSs. Their findings are naturally not as encompassing as those from the multitude of studies done on lead-based perovskite HSs. However, their study presents an important step towards sustainable implementation of TMDC/PM HSs and it will be interesting to see future work going deeper into the comparison of lead-based and lead-free perovskite/TMDC HSs.

4.4. Exciton- and energy transfer

PL lifetimes can also yield insight into the possible formation of IEs and whether charge or energy transfer occurs in a TMDC/perovskite HS. For example, room-temperature TRPL and fluorescence lifetime imaging microscopy measurements of organic–inorganic heterostructures found that the average PL lifetime of the $CsPbBr_{3-x}I_x$ QDs was 16.7 ns, which reduced to 6.2 ns in the MoS_2/ $CsPbBr_{3-x}I_x$ HS, while the average PL lifetime of $MAPbBr_3$ reduced from 11.2 ns in the pristine sample to 2.9 ns in the HS [175]. This reduction was attributed to the charge extraction kinetics of the HS.

Further insights into interfacial dynamics can be obtained by varying the interfacial width, and evaluating its effect on the charge transfer dynamics. By either decreasing the thickness of MoS_2 or removing insulating hBN layers between the materials [80], the PL lifetime of the perovskite QDs decreases (figure 9), indicating the presence of an additional relaxation channel. Panel (c) of figure 9 shows the TRPL data for varying MoS_2 layer thickness, and panel (d) the extracted thickness-dependent relaxation rate, which saturates for thicknesses of around 10 MoS_2 layers, approaching the value of the isolated QDs. Panels (e) and (f) reveal a similar behaviour for the thickness of an hBN spacer layer between the QDs and an MoS_2 monolayer. This decrease of the QD PL lifetime suggests the emergence of additional non-radiative relaxation channels that become activated for lower energy barriers or when the band-alignment of the two compounds becomes more favourable due to thin MoS_2 as opposed to thicker MoS_2. This thickness-dependent PL lifetime thus points to the presence of charge transfer across the HS.

4.5. Signs of interlayer excitons?

Ultrafast spectroscopic characterisation thus presents a powerful tool to study the kinetics and determine rates of charge- and energy transfer in TMDC/perovskite HSs. It is therefore interesting to ask whether similar to TMDC/TMDC HSs, there have been signs of spatially separated IEs in mixed HSs as well. The studies towards this topic are few in the mixed TMDC/PM HS. Nevertheless, an interesting study was presented by Li *et al*, who performed a full analysis of the charge dynamics across a $WS_2/CsPbBr_3$ QD HS using a combination of femtosecond TA spectroscopy and room-temperature steady-state PL [184]. The TA signal showed photobleaching (PB) proportional to the exciton fluence and photoabsorption (PA) due to biexcitons and other pump-induced absorbing states, see figure 10(a). The quenching of the PB signal suggests that few excitons remain in the QDs after excitation. Additionally, the PB signal of the A-exciton resonance was enhanced, suggesting that the excitons generated in the perovskite were immediately transferred to the TMDC. To pin down the

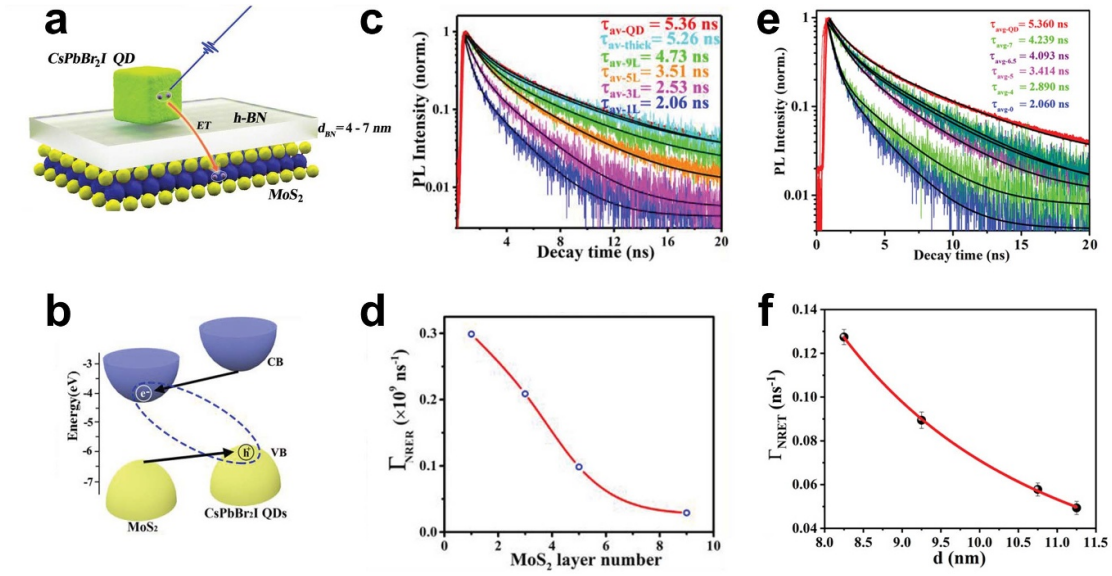

Figure 9. (a) Schematic and (b) band alignment of the monolayer MoS_2 and 8.5 nm sized $CsPbBr_2I$ nanocrystals HS studied by Luo and co-workers. (c) Room-temperature TRPL spectra of the HS with additional MoS_2 layers. (d) The corresponding non-radiative relaxation rate as a function of the increasing number of MoS_2 layers. (e) TRPL spectra of the HS with increasing hBN spacer thickness. (f) The corresponding non-radiative relaxation rate as a function of the hBN spacer thickness. [80] John Wiley & Sons. © 2019 WILEY-VCH Verlag GmbH & Co. KGaA, Weinheim.

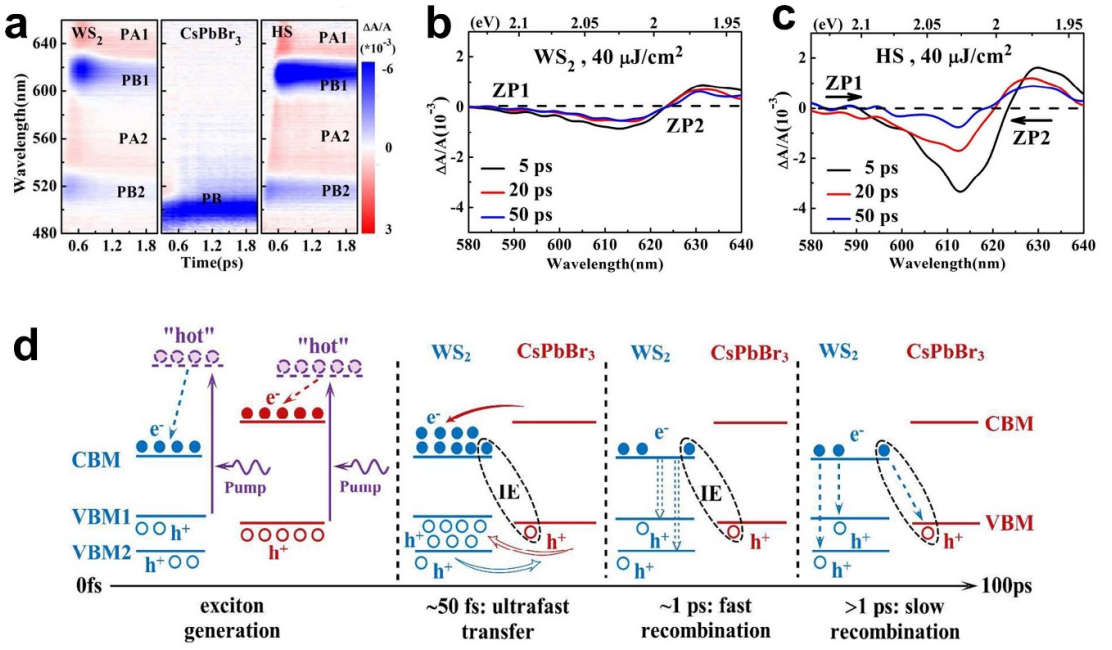

Figure 10. (a) Transient absorption spectroscopy with photobleaching (PB) and photo-induced absorption (PA) signals labelled for the monolayer WS_2, 11 nm sized-$CsPbBr_3$ nanocrystals pristine samples and the $WS_2/CsPbBr_3$ HS. PB1 (PB2) refers to the PB signals of the *A* (*B*) excitons. (b) TA signal of the *A* exciton resonance of the WS_2 structure. (c) TA signal of the *A* exciton resonance of the HS. Note the evolution of the ZP and the enhanced PA effect in the HS compared to the pristine sample. (d) Kinetic model of the ultra-fast charge processes of the HS. Reproduced from [184] with permission from the Royal Society of Chemistry.

competitive processes behind the PB and PA features, 'zero-points' (ZP) were defined at probe wavelength positions where the photo-induced absorption vanished (vanishing ΔA in figures 10(b) and (c). In the HS, these ZPs shift over time towards an increased PA feature, indicating the formation of a built-in electric field due to IEs across the HS, which in turn altered the resonances of the excitons in the WS_2 layer. This concept had previously been described by He and co-workers for a WS_2/graphene HS [190], and here could be developed into a full model of the recombination dynamics and fitted to the TA signal for fast and slow recombination processes as depicted in figure 10(d).

4.6. Further considerations

In addition to the above examples of thin films or QDs of lead halide perovskites with ABX_3 structure, 2D Ruddleston–Popper perovskites, with a structure of $A_{n+1}B_nX_{3n+1}$ are also widely employed as one of the layers in TMDC/perovskite HS [187, 191–193]. As an example, excitonic energy transfer has been observed in the quasi-hybrid perovskite $C_6H_5C_2H_4NH_3$ (PEPI)/WS_2 HS, with the PEPI being around 100 nm thick and monolayer WS_2 [187]. Experimental evidence for the energy transfer was presented using PL, PLE and reflectance spectroscopy techniques. In the PLE measurements performed at 110 K, the authors observed that the A exciton PL from WS_2 is enhanced at the excitation energy corresponding to the exciton of PEPI, indicating energy transfer between the two compounds had occurred. Overall, while many initial works have been performed on these mixed HSs, important details of the fundamental processes are yet to be uncovered. For example, many tuning parameters have been discussed above, but it is not always clear how these tuning parameters affect the time dynamics of charge transfer. To gain further insight, the optical experimental methods described above should be supplemented by further optical measurements such as reflectance spectroscopy, and other physical characterisation methods such as x-ray diffraction, TEM, and atomic force microscopy, and by theoretical analyses. In this regard, a theoretical study using time-dependent DFT points to yet another factor in band alignments [194]. The authors found that the exact crystal facet of $CsPbBr_3$ nanocrystals exposed to the TMDC can alter the band alignment and suggested that this can be an alternative explanation for mixed band-alignment, besides the spin–orbit splitting mechanism proposed by Bauer *et al* [174]. This interpretation is still discussed in the follow-up theoretical work by Liao *et al*, who found a type II alignment for both crystal facets in the same system [195]. Subsequently, Xu *et al* stressed that the different crystal facets of $CsPbBr_3$ do result in different band alignment types with MoS_2, as long as the SOC is included to describe the properties of the perovskite [196]. Similar work has been undertaken on the $CsPbBr_3/MoSe_2$ system, where both perovskite facets show a type II alignment with the TMDC [197]. Finally, also in the case of the $CsPbI_3/MoS_2$ and $CsPbI_3/WS_2$ systems, the alignment turns out to be of type II, independent of the perovskite facet exposed to the TMDC. This shows that for some specific combinations, such as $CsPbBr_3/MoS_2$, the band alignment is so close between type I and type II that the specifics of crystal facets, and SOC start to become important [198]. It will be interesting to see how these effects, and the aforementioned tuning parameters, overlap in less-than-ideal macroscopic samples and practical situations.

Before we address the alternative processes that may be occurring in TMDC/TMDC and TMDC/PM HSs, we summarise the key experimental reports that we have previously discussed regarding TMDC/PM HSs in table 1.

5. Alternative processes

While the aforementioned features such as the additional low-energy, long-lived PL and quenching of the excitonic peaks of both HS components have been attributed to charge transfer between the materials and the formation of the IE, alternative processes are also imaginable. In principle, the additional PL emission peaks, PL quenching, prolonged lifetimes and even unusual TA signals can all be attributed to entirely different processes. For example, the formation of radiative defect states in the HS can result in a change in the average lifetime and can be recorded as a low-energy PL signal. It is therefore crucial to differentiate such spectroscopic peculiarities from IE formation and recombination processes in TMDC HSs.

In fact, TMDC monolayers can have an array of intrinsic point defects, grain boundaries, surface defects, vacancies and adatoms; these defects and their densities can vary across different materials and different fabrication procedures [64, 119, 120]. These intrinsic defects can alter the PL, band gaps and recombination lifetimes, where the defect-assisted recombination typically triggers Auger recombination in such monolayers [63, 199, 200]. Furthermore, the substrate can contribute to the variation of the monolayers' and HSs' optical properties. For example, PL quenching has been shown to occur when TMDC monolayers were grown on graphene compared to their PL emission when fabricated on rigid substrates [201–203]. Furthermore, PL quenching may simply be a result of less overall irradiation of the sample when in an HS configuration compared to a pristine sample. Optical spectroscopic tools, as described above, along with scanning electron microscopy (SEM), TEM, XPS, secondary-ion mass spectrometry (SIMS) and other physical characterisation techniques, combined with density functional theory (DTF) and electron energy-loss spectroscopy (EELs) calculations provide a means to analyse such defects and differentiate between different mechanisms [82, 83].

Some, albeit not all, works that analyse TMDC/TMDC and TMDC/perovskite HS also consider alternative mechanisms that could explain their spectroscopic results. For example, Bauer and coworkers considered that the PL quenching of WS_2 in their TMDC/perovskite HS could simply be due to the excitation from the laser not reaching the WS_2, due to their $MAPbI_3$ layer being 100 nm thick [174]. They addressed this consideration by fabricating the HS on a transparent (sapphire) substrate and

Table 1. Summary of the experimental works discussed in this literature review which characterise various TMDC/PM heterostructure materials using various key optical methods. These tabulated works also explicitly identify the heterostructure type and describe evidence for either charge transfer, energy transfer, or both. Abbreviations: BA = butylamine, N.D. = not described, Abs. = UV–VIS absorption spectroscopy, TRPL = time-resolved photoluminescence spectroscopy, TAS = transient absorption spectroscopy, DRS = differential reflection spectroscopy.

TMDC/perovskite	Perovskite type	HS type	Transfer type	Key optical techniques	Year	Reference
$WS_2/CsPbBr_3$	Microplates	Type II	Charge	Abs., PL, Raman	2018	[101]
$MoSe_2/CsPbBr_3$	Nanocrystals	Type I	Energy	Abs., PL, TRPL	2022	[153]
$WSe_2/CsPbBr_3$	Thin film	Type I	Energy	Abs., PL, TAS	2021	[166]
$MoS_2/CsPbBr_3$	Thin film	Type II	Charge	Abs., PL, TAS, TRPL	2022	[167]
$WS_2/CsPbBr_3$	Thin film	Type II	Charge	Abs., PL, TAS, TRPL	2022	[167]
$MoS_2/MAPbI_3$	Thin film	Type II	Charge	PL, TAS, Abs., Raman	2016	[171]
$WS_2/MAPbI_3$	Thin Film	Type I	Charge	Abs., PL, TAS, DRS	2018	[174]
$MoS_2/CsPbBr_{3-x}I_x$	Quantum dots	Type II	Charge	Raman, PL, TRPL	2018	[175]
$MoS_2/MAPbBr_3$	Quantum dots	Type I	Energy	Raman, PL, TRPL	2018	[175]
$MoS_2/CsPbBr_3$	Nanosheets	Type II	Charge	Abs., PL, TRPL	2018	[176]
$WS_2/CsPbI_3$	Nanocrystals	Type II	Charge	Abs., PL, TRPL, Raman	2023	[180]
$MoS_2/CsPbI_{3-x}Br_x$	Quantum dots	Type II	Charge	Raman, Abs., PL, TRPL	2018	[181]
$MoS_2/Cs_{0.85}FA_{0.15}PbBr_3$	Quantum dots	N.D.	Charge	Raman, Abs., PL	2022	[182]
$MoS_2/CsPbBr_3$	Nanowire	Type I	Energy	Raman, PL, TRPL, TAS	2018	[183]
$WSe_2/CsPbBr_3$	Nanowire	Type II	Charge	Raman, PL, TRPL, TAS	2018	[183]
$WS_2/CsPbBr_3$	Quantum dots	Hybrid I/II	Charge	TAS, PL, Raman	2018	[184]
$MoS_2/CsPbI_{3-x}Br_x$	Quantum dots	Type II	Charge	Abs., PL, TRPL, Raman	2019	[185]
$WS_2/(C_6H_5C_2H_4NH_3)_2PbI_4$	Quasi-2D flakes	Type II	Energy	DRS, PL, PLE, Raman	2020	[187]
$MoS_2/CsPbBr_3$	Quantum dots	Type II	Charge	Abs., PL, TAS, Raman, TRPL	2020	[188]
$WS_2/CsSnBr_3$	Thin Film	Type II	Charge	Raman, Abs., PL, TRPL	2023	[189]
$WSe_2/(C_4H_9NH_3)_2PbI_4$	2D Microplates	Type II	Charge	PL, Raman	2020	[191]
$WS_2/(C_6H_5C_2H_4NH_3)_2PbI_4$	2D single crystals	Type II	Charge	DRS, PL	2020	[192]
$WS_2/(BA)_2(MA)_3Pb_4I_{13}$	2D bulk crystals	Type I	Charge	Raman, PL, PLE, TRPL	2019	[193]

illuminating the structure from the backside. In both cases, WS_2 PL was quenched, showing that reduced absorption in the WS_2 layer was not the reason for PL quenching.

Rivera and co-workers partially omitted the possibility of defect states formed in $MoSe_2/WSe_2$ HS by fabricating homostructures using the TMDC monolayers and finding that the signature IE signals in the HS could not be reproduced in the homostructures [14].

Similarly, Chen and co-workers considered that the low-energy PL peak in the 2D perovskite/TMDC HS could arise from laser-induced defect states. To exclude this possibility, temperature-, power- and excitation-energy-dependent steady-state PL measurements were conducted on the isolated perovskite, which would have been expected to thermally degrade and reproduce the broadened peak observed in the HS; yet, this peak was not observed in isolation, indicating that thermal degradation does not occur. Furthermore, to verify that the excitonic emission quenching originated from charge transfer, they inserted an insulating 6 nm thick hBN layer between the TMDC and perovskite layers and showed that the excitonic emission of the monolayers was not quenched, as no charge was transferred. They stacked the layers in an inverse order to show that the exciton emission had been present regardless of stacking sequence and varied the TMDC employed to show that IEs were formed in similar type II band alignment configurations, verifying that the IE signals were reproducible under different configurations [191].

While the above-mentioned works refute the formation of defect states and possible changes in the HS, other works do find clear signatures of them. Concerning the latter, the work of Mohite and Atwater on a 7.5 nm thick 2D perovskite and a bilayer WS_2 HS is noteworthy [193]. They observed broadened PL peaks at low temperatures for different 2D perovskite/WS_2 HSs which were directly attributed to emissive defect states, as these peaks were not present at higher temperatures. The defect states in both the TMDC bilayer and the HS were further confirmed using differential reflection spectroscopy. Wu and co-workers fabricated PFETs from the perovskite QD/TMDC HS and attributed the measured photogating effect to trapped long-lifetime carriers in the surface states or interface trap states [175]. This effect was also observed in TMDC monolayers [204, 205]. Additional reports also have shown that PL emission observed can be directly from defect states of the bilayers of samples [193, 206–208]. These experiments verify that indeed such HSs can exhibit surface defect states that can interfere with the optoelectronic characteristics, making a thorough characterisation using complementary optical and structural analysis indispensable.

6. Conclusions

TMDC monolayers are intriguing materials due to their enhanced optical properties and strong excitonic effects. Despite intense studies, this class of semiconducting materials still holds promise for exciting developments, especially towards the optoelectronic properties of less well-known compounds such as the Re, Zr, Hf dichalcogenides, alloys and Janus monolayers. Even for the more well-known Mo and W dichalcogenides, a whole zoo of materials is left to explore once they are combined in HSs. Specifically, the stacking-angle dependence on their optoelectronic properties is an active field of research. The formation of IEs is especially exciting because these long-lived states have a more diverse set of tuning parameters than the excitons formed within the layers. In this regard, it will be of interest to investigate the interplay between electron- and hole wavefunction overlaps and the momentum-indirect nature of IE transitions. The latter aspect is especially intriguing as it could point to an as-of-yet under-investigated tuning parameter. In this regard, the common molybdenum- and tungsten-based TMDC HSs all show similar behaviour where the individual electron and holes seem to reside in different valleys of momentum space. However, combinations with the aforementioned Re and other transition-metal materials offer fresh alternatives and it will be intriguing to study the effects of different k-space transitions in HSs of these new compounds.

Further degrees of freedom exist in the emerging field of mixed HSs, which we have reviewed here with a focus on TMDC/perovskite HSs. Since the perovskites are easily tunable by composition, dimensionality and surface chemistry, the possible combinations, and tuning parameters, for HSs with TMDC monolayers are vast. We believe that, while all works discussed here are interesting on their own, systematic investigations of the interplay of all these factors are still missing. Because of the complexity of these structures, future works must adapt and expand on the current spectroscopic techniques as single measurements alone are insufficient for reaching conclusions. Furthermore, optical spectroscopic characterisation methods should be combined with physical and chemical analyses, along with theoretical calculations and interpretations, to attain a full dynamical model of each potential HS. It is tempting to neglect alternative defect state processes and other mechanisms when interpreting the measured optical features. These alternative considerations need to be included in future works on TMDC heterobilayer analysis, to achieve a full picture of the processes within the HS.

The 2D TMDC HS research field is still relatively young, and the progress in the understanding of IEs and the overall charge dynamics in TMDC HSs is impressive. Experimental optical characterisation methods have been key in driving these developments and continue to do so. One thing completely neglected in this review is the possibility of stacking more than two layers, which widens the scope of combinations even further. Overall, the TMDC HSs are full of possibilities, and it will be interesting to see future device applications come out of this highly interesting field.

Data availability statement

No new data were created or analysed in this study.

Acknowledgments

This research received funding from the Netherlands Organisation for Scientific Research (NWO) in the framework of the Materials for Sustainability Programme (MAT4SUS Project No. 739.017.011).

ORCID iDs

Sarah C Gillespie https://orcid.org/0009-0005-8124-0616
Marco van der Laan https://orcid.org/0000-0001-9571-3190
Sachin Kinge https://orcid.org/0000-0002-9149-7440
Peter Schall https://orcid.org/0000-0003-2612-2762

References

[1] Schulman D S, Arnold A J, Razavieh A, Nasr J and Das S 2017 The prospect of two-dimensional heterostructures: a review of recent breakthroughs *IEEE Nanotechnol. Mag.* **11** 6–17
[2] Wang J, Li Z, Chen H, Deng G and Niu X 2019 Recent advances in 2D lateral heterostructures *Nano Micro Lett.* **11** 1–31
[3] Carvalho A, Ribeiro R and Neto A C 2013 Band nesting and the optical response of two-dimensional semiconducting transition metal dichalcogenides *Phys. Rev.* B **88** 115205
[4] Kozawa D *et al* 2014 Photocarrier relaxation pathway in two-dimensional semiconducting transition metal dichalcogenides *Nat. Commun.* **5** 4543
[5] Hanbicki A, Currie M, Kioseoglou G, Friedman A and Jonker B 2015 Measurement of high exciton binding energy in the monolayer transition-metal dichalcogenides WS_2 and WSe_2 *Solid State Commun.* **203** 16–20
[6] Lan C, Li C, Wang S, He T, Zhou Z, Wei D, Guo H, Yang H and Liu Y 2017 Highly responsive and broadband photodetectors based on WS_2–graphene van der Waals epitaxial heterostructures *J. Mater. Chem.* **5** 1494–500
[7] Wu E, Wu D, Jia C, Wang Y, Yuan H, Zeng L, Xu T, Shi Z, Tian Y and Li X 2019 *In situ* fabrication of 2D WS_2/Si type-II heterojunction for self-powered broadband photodetector with response up to mid-infrared *ACS Photonics* **6** 565–72
[8] Ghosh J and Giri P 2021 Recent advances in perovskite/2D materials based hybrid photodetectors *J. Phys. Mater.* **4** 032008
[9] Cheng R, Li D, Zhou H, Wang C, Yin A, Jiang S, Liu Y, Chen Y, Huang Y and Duan X 2014 Electroluminescence and photocurrent generation from atomically sharp WSe_2/MoS_2 heterojunction *p–n* diodes *Nano Lett.* **14** 5590–7

[10] Som D, Trivedi S, Chatterjee A and Kanungo S 2021 Van der Waals (vdW) heterostructures based on transition metal dichalcogenides (TMD): current status and prospects in broadband photodetector applications *Microelectronics and Signal Processing* 1st edn (CRC Press) pp 1–16

[11] Li C, Cao Q, Wang F, Xiao Y, Li Y, Delaunay J-J and Zhu H 2018 Engineering graphene and TMDS based van der Waals heterostructures for photovoltaic and photoelectrochemical solar energy conversion *Chem. Soc. Rev.* **47** 4981–5037

[12] Furchi M M, Zechmeister A A, Hoeller F, Wachter S, Pospischil A and Mueller T 2016 Photovoltaics in van der Waals heterostructures *IEEE J. Sel. Top. Quantum Electron.* **23** 106–16

[13] Fang H *et al* 2014 Strong interlayer coupling in van der Waals heterostructures built from single-layer chalcogenides *Proc. Natl Acad. Sci.* **111** 6198–202

[14] Rivera P *et al* 2015 Observation of long-lived interlayer excitons in monolayer $MoSe_2$–WSe_2 heterostructures *Nat. Commun.* **6** 6242

[15] Wu L, Chen Y, Zhou H and Zhu H 2019 Ultrafast energy transfer of both bright and dark excitons in 2D van der Waals heterostructures beyond dipolar coupling *ACS Nano* **13** 2341–8

[16] Mueller T and Malic E 2018 Exciton physics and device application of two-dimensional transition metal dichalcogenide semiconductors *npj 2D Mater. Appl.* **2** 29

[17] Chhowalla M, Shin H S, Eda G, Li L-J, Loh K P and Zhang H 2013 The chemistry of two-dimensional layered transition metal dichalcogenide nanosheets *Nat. Chem.* **5** 263–75

[18] Islam M A *et al* 2022 Exfoliation mechanisms of 2D materials and their applications *Appl. Phys. Rev.* **9** 041301

[19] Hao W, Marichy C and Journet C 2018 Atomic layer deposition of stable 2D materials *2D Mater.* **6** 012001

[20] Muratore C, Voevodin A A and Glavin N R 2019 Physical vapor deposition of 2D van der Waals materials: a review *Thin Solid Films* **688** 137500

[21] Huo C, Yan Z, Song X and Zeng H 2015 2D materials via liquid exfoliation: a review on fabrication and applications *Sci. Bull.* **60** 1994–2008

[22] Liu Y, Zhang S, He J, Wang Z M and Liu Z 2019 Recent progress in the fabrication, properties and devices of heterostructures based on 2D materials *Nano Micro Lett.* **11** 1–24

[23] Xu X, Guo T, Kim H, Hota M K, Alsaadi R S, Lanza M, Zhang X and Alshareef H N 2022 Growth of 2D materials at the wafer scale *Adv. Mater.* **34** 2108258

[24] Cai Z, Liu B, Zou X and Cheng H-M 2018 Chemical vapor deposition growth and applications of two-dimensional materials and their heterostructures *Chem. Rev.* **118** 6091–133

[25] Zhang Z, Wang S, Liu X, Chen Y, Su C, Tang Z, Li Y and Xing G 2021 Metal halide perovskite/2D material heterostructures: syntheses and applications *Small Methods* **5** 2000937

[26] Wilson J A and Yoffe A 1969 The transition metal dichalcogenides discussion and interpretation of the observed optical, electrical and structural properties *Adv. Phys.* **18** 193–335

[27] Mak K F, Lee C, Hone J, Shan J and Heinz T F 2010 Atomically thin MoS_2: a new direct-gap semiconductor *Phys. Rev. Lett.* **105** 136805

[28] Novoselov K S, Mishchenko A, Carvalho O A and Castro Neto A 2016 2D materials and van der Waals heterostructures *Science* **353** aac9439

[29] Mak K F and Shan J 2016 Photonics and optoelectronics of 2D semiconductor transition metal dichalcogenides *Nat. Photon.* **10** 216–26

[30] Wang G, Chernikov A, Glazov M M, Heinz T F, Marie X, Amand T and Urbaszek B 2018 Colloquium: excitons in atomically thin transition metal dichalcogenides *Rev. Mod. Phys.* **90** 021001

[31] Manzeli S, Ovchinnikov D, Pasquier D, Yazyev O V and Kis A 2017 2D transition metal dichalcogenides *Nat. Rev. Mater.* **2** 1–15

[32] Zhu Z Y, Cheng Y C and Schwingenschlögl U 2011 Giant spin-orbit-induced spin splitting in two-dimensional transition-metal dichalcogenide semiconductors *Phys. Rev.* B **84** 153402

[33] Kormányos A, Burkard G, Gmitra M, Fabian J, Zólyomi V, Drummond N D and Fal'ko V 2015 k·p theory for two-dimensional transition metal dichalcogenide semiconductors *2D Mater.* **2** 022001

[34] Li T and Galli G 2007 Electronic properties of MoS_2 nanoparticles *J. Phys. Chem.* C **111** 16192–6

[35] Kam K and Parkinson B 1982 Detailed photocurrent spectroscopy of the semiconducting group VIB transition metal dichalcogenides *J. Phys. Chem.* **86** 463–7

[36] Yao W, Xiao D and Niu Q 2008 Valley-dependent optoelectronics from inversion symmetry breaking *Phys. Rev.* B **77** 235406

[37] Xiao D, Liu G-B, Feng W, Xu X and Yao W 2012 Coupled spin and valley physics in monolayers of MoS_2 and other group-VI dichalcogenides *Phys. Rev. Lett.* **108** 196802

[38] Yu T and Wu M 2014 Valley depolarization due to intervalley and intravalley electron-hole exchange interactions in monolayer MoS_2 *Phys. Rev.* B **89** 205303

[39] Yan T, Qiao X, Tan P and Zhang X 2015 Valley depolarization in monolayer WSe_2 *Sci. Rep.* **5** 15625

[40] Echeverry J, Urbaszek B, Amand T, Marie X and Gerber I C 2016 Splitting between bright and dark excitons in transition metal dichalcogenide monolayers *Phys. Rev.* B **93** 121107

[41] Zhang X-X *et al* 2017 Magnetic brightening and control of dark excitons in monolayer WSe_2 *Nat. Nanotechnol.* **12** 883–8

[42] Arora A, Koperski M, Nogajewski K, Marcus J, Faugeras C and Potemski M 2015 Excitonic resonances in thin films of WSe_2: from monolayer to bulk material *Nanoscale* **7** 10421–9

[43] Arora A, Nogajewski K, Molas M, Koperski M and Potemski M 2015 Exciton band structure in layered $MoSe_2$: from a monolayer to the bulk limit *Nanoscale* **7** 20769–75

[44] Splendiani A, Sun L, Zhang Y, Li T, Kim J, Chim C-Y, Galli G and Wang F 2010 Emerging photoluminescence in monolayer MoS_2 *Nano Lett.* **10** 1271–5

[45] Komsa H-P and Krasheninnikov A V 2012 Effects of confinement and environment on the electronic structure and exciton binding energy of MoS_2 from first principles *Phys. Rev.* B **86** 241201

[46] Berkelbach T C, Hybertsen M S and Reichman D R 2013 Theory of neutral and charged excitons in monolayer transition metal dichalcogenides *Phys. Rev.* B **88** 045318

[47] Elliott R 1957 Intensity of optical absorption by excitons *Phys. Rev.* **108** 1384

[48] Ye Z, Cao T, O'brien K, Zhu H, Yin X, Wang Y, Louie S G and Zhang X 2014 Probing excitonic dark states in single-layer tungsten disulphide *Nature* **513** 214–8

[49] Zhang X, Shan W-Y and Xiao D 2018 Optical selection rule of excitons in gapped chiral fermion systems *Phys. Rev. Lett.* **120** 077401

[50] Chernikov A, Berkelbach T C, Hill H M, Rigosi A, Li Y, Aslan B, Reichman D R, Hybertsen M S and Heinz T F 2014 Exciton binding energy and nonhydrogenic rydberg series in monolayer WS_2 *Phys. Rev. Lett.* **113** 076802

[51] Mak K F, He K, Lee C, Lee G H, Hone J, Heinz T F and Shan J 2013 Tightly bound trions in monolayer MoS_2 *Nat. Mater.* **12** 207–11

[52] Jones A M *et al* 2013 Optical generation of excitonic valley coherence in monolayer WSe_2 *Nat. Nanotechnol.* **8** 634–8

[53] You Y, Zhang X-X, Berkelbach T C, Hybertsen M S, Reichman D R and Heinz T F 2015 Observation of biexcitons in monolayer WSe_2 *Nat. Phys.* **11** 477–81

[54] Sie E J, Frenzel A J, Lee Y-H, Kong J and Gedik N 2015 Intervalley biexcitons and many-body effects in monolayer MoS_2 *Phys. Rev.* B **92** 125417

[55] Saigal N and Ghosh S 2015 H-point exciton transitions in bulk MoS_2 *Appl. Phys. Lett.* **106** 182103

[56] Li Z *et al* 2019 Emerging photoluminescence from the dark-exciton phonon replica in monolayer WSe_2 *Nat. Commun.* **10** 2469

[57] Liu E, van Baren J, Taniguchi T, Watanabe K, Chang Y-C and Lui C H 2019 Valley-selective chiral phonon replicas of dark excitons and trions in monolayer WSe_2 *Phys. Rev. Res.* **1** 032007

[58] Munkhbat B, Baranov D G, Stührenberg M, Wersäll M, Bisht A and Shegai T 2018 Self-hybridized exciton-polaritons in multilayers of transition metal dichalcogenides for efficient light absorption *ACS Photonics* **6** 139–47

[59] Mitterreiter E *et al* 2021 The role of chalcogen vacancies for atomic defect emission in MoS_2 *Nat. Commun.* **12** 3822

[60] Jiang H 2011 Structural and electronic properties of ZrX_2 and HfX_2 (X = S and Se) from first principles calculations *J. Chem. Phys.* **134** 204705

[61] Ho C, Huang Y and Tiong K-K 2001 In-plane anisotropy of the optical and electrical properties of ReS_2 and $ReSe_2$ layered crystals *J. Alloys Compd.* **317** 222–6

[62] Moody G, Schaibley J and Xu X 2016 Exciton dynamics in monolayer transition metal dichalcogenides *J. Opt. Soc. Am.* B **33** C39–C49

[63] Wang H, Zhang C and Rana F 2015 Ultrafast dynamics of defect-assisted electron–hole recombination in monolayer MoS_2 *Nano Lett.* **15** 339–45

[64] Zhou W, Zou X, Najmaei S, Liu Z, Shi Y, Kong J, Lou J, Ajayan P M, Yakobson B I and Idrobo J-C 2013 Intrinsic structural defects in monolayer molybdenum disulfide *Nano Lett.* **13** 2615–22

[65] Jeong H Y, Jin Y, Yun S J, Zhao J, Baik J, Keum D H, Lee H S and Lee Y H 2017 Heterogeneous defect domains in single-crystalline hexagonal WS_2 *Adv. Mater.* **29** 1605043

[66] Hong J *et al* 2015 Exploring atomic defects in molybdenum disulphide monolayers *Nat. Commun.* **6** 6293

[67] Yuan L and Huang L 2015 Exciton dynamics and annihilation in WS_2 2D semiconductors *Nanoscale* **7** 7402–8

[68] Sun Y, Wang D and Shuai Z 2016 Indirect-to-direct band gap crossover in few-layer transition metal dichalcogenides: a theoretical prediction *J. Phys. Chem.* C **120** 21866–70

[69] Voshell A, Terrones M and Rana M 2020 Thermal and photo sensing capabilities of mono-and few-layer thick transition metal dichalcogenides *Micromachines* **11** 693

[70] Shestakova A, Lavrov S, Mishina E and Efimenkov Y R 2017 Highly sensitive photodetector based on transition metal dichalcogenides monolayer *2017 Progress in Electromagnetics Research Symp.-Spring* (*PIERS*) (IEEE) pp 2845–7

[71] Tsai M-L, Su S-H, Chang J-K, Tsai D-S, Chen C-H, Wu C-I, Li L-J, Chen L-J and He J-H 2014 Monolayer MoS_2 heterojunction solar cells *ACS Nano* **8** 8317–22

[72] Wu K, Ma H, Gao Y, Hu W and Yang J 2019 Highly-efficient heterojunction solar cells based on two-dimensional tellurene and transition metal dichalcogenides *J. Mater. Chem.* A **7** 7430–6

[73] Kumar A, Yagodkin D, Stetzuhn N, Kovalchuk S, Melnikov A, Elliott P, Sharma S, Gahl C and Bolotin K I 2021 Spin/valley coupled dynamics of electrons and holes at the MoS_2–$MoSe_2$ interface *Nano Lett.* **21** 7123–30

[74] Jiang Y, Chen S, Zheng W, Zheng B and Pan A 2021 Interlayer exciton formation, relaxation and transport in TMD van der Waals heterostructures *Light Sci. Appl.* **10** 72

[75] Singh S *et al* 2023 Valley-polarized interlayer excitons in 2D chalcogenide–halide perovskite–van der Waals heterostructures *ACS Nano* **17** 7487–97

[76] Liaov M *et al* 2020 Precise control of the interlayer twist angle in large scale MoS_2 homostructures *Nat. Commun.* **11** 2153

[77] Geim A K and Grigorieva I V 2013 Van der waals heterostructures *Nature* **499** 419–25

[78] Liu P and Xiang B 2017 2D hetero-structures based on transition metal dichalcogenides: fabrication, properties and applications *Sci. Bull.* **62** 1148–61

[79] Hook D W, Porter S J and Herzog C 2018 Dimensions: building context for search and evaluation *Front. Res. Metrics Anal.* **3** 23

[80] Liu H, Wang C, Wang T, Hu X, Liu D and Luo J 2019 Controllable interlayer charge and energy transfer in perovskite quantum dots/transition metal dichalcogenide heterostructures *Adv. Mater. Interfaces* **6** 1901263

[81] Lin Z, Carvalho B R, Kahn E, Lv R, Rao R, Terrones H, Pimenta M A and Terrones M 2016 Defect engineering of two-dimensional transition metal dichalcogenides *2D Mater.* **3** 022002

[82] Liang Q, Zhang Q, Zhao X, Liu M and Wee A T 2021 Defect engineering of two-dimensional transition-metal dichalcogenides: applications, challenges and opportunities *ACS Nano* **15** 2165–81

[83] Kim S-Y, Kim J H, Lee S, Kwak J, Jo Y, Yoon E, Lee G-D, Lee Z and Kwon S-Y 2018 The impact of substrate surface defects on the properties of two-dimensional van der Waals heterostructures *Nanoscale* **10** 19212–9

[84] Yan R *et al* 2015 Esaki diodes in van der Waals heterojunctions with broken-gap energy band alignment *Nano Lett.* **15** 5791–8

[85] Lei C, Ma Y, Xu X, Zhang T, Huang B and Dai Y 2019 Broken-gap type-III band alignment in WTe_2/HfS_2 van der Waals heterostructure *J. Phys. Chem.* C **123** 23089–95

[86] Cong X, Zheng Y, Huang F, You Q, Tang J, Fang F, Jiang K, Han C and Shi Y 2022 Efficiently band-tailored type-III van der Waals heterostructure for tunnel diodes and optoelectronic devices *Nano Res.* **15** 8442–50

[87] Zhang C *et al* 2016 Systematic study of electronic structure and band alignment of monolayer transition metal dichalcogenides in van der Waals heterostructures *2D Mater.* **4** 015026

[88] Ravi V K, Markad G B and Nag A 2016 Band edge energies and excitonic transition probabilities of colloidal $CsPbX_3$ (X = Cl, Br, I) perovskite nanocrystals *ACS Energy Lett.* **1** 665–71

[89] Walsh A 2015 Principles of chemical bonding and band gap engineering in hybrid organic–inorganic halide perovskites *J. Phys. Chem.* C **119** 5755–60

[90] Hedin L 1965 New method for calculating the one-particle green's function with application to the electron-gas problem *Phys. Rev.* **139** A796

[91] Godby R W, Schlüter M and Sham L 1988 Self-energy operators and exchange-correlation potentials in semiconductors *Phys. Rev.* B **37** 10159

[92] Aryasetiawan F and Gunnarsson O 1998 The *GW* method *Rep. Prog. Phys.* **61** 237

[93] Chiu M-H, Zhang C, Shiu H-W, Chuu C-P, Chen C-H, Chang C, Chen C, Chou M, Shih C and Li L 2014 Determination of band alignment in transition metal dichalcogenides heterojunctions (arXiv:1406.5137)

[94] Franciosi A and Van de Walle C G 1996 Heterojunction band offset engineering *Surf. Sci. Rep.* **25** 1–140

[95] Wilson N R *et al* 2017 Determination of band offsets, hybridization and exciton binding in 2D semiconductor heterostructures *Sci. Adv.* **3** e1601832

[96] Xu K *et al* 2018 The role of Anderson's rule in determining electronic, optical and transport properties of transition metal dichalcogenide heterostructures *Phys. Chem. Chem. Phys.* **20** 30351–64

[97] Chiu M-H, Zhang C, Shiu H-W, Chuu C-P, Chen C-H, Chang C-Y S, Chen C-H, Chou M-Y, Shih C-K and Li L-J 2015 Determination of band alignment in the single-layer MoS_2/WSe_2 heterojunction *Nat. Commun.* **6** 7666

[98] Wang G, Bouet L, Lagarde D, Vidal M, Balocchi A, Amand T, Marie X and Urbaszek B 2014 Valley dynamics probed through charged and neutral exciton emission in monolayer WSe_2 *Phys. Rev.* B **90** 075413

[99] Mouri S, Zhang W, Kozawa D, Miyauchi Y, Eda G and Matsuda K 2017 Thermal dissociation of inter-layer excitons in $MoS_2/MoSe_2$ hetero-bilayers *Nanoscale* **9** 6674–9

[100] Liu Y, Fang H, Rasmita A, Zhou Y, Li J, Yu T, Xiong Q, Zheludev N, Liu J and Gao W 2019 Room temperature nanocavity laser with interlayer excitons in 2D heterostructures *Sci. Adv.* **5** eaav4506

[101] Yan Z-Z, Jiang Z-H, Lu J-P and Ni Z-H 2018 Interfacial charge transfer in WS_2 monolayer/$CsPbBr_3$ microplate heterostructure *Front. Phys.* **13** 1–7

[102] Karni O *et al* 2019 Infrared interlayer exciton emission in MoS_2/WSe_2 heterostructures *Phys. Rev. Lett.* **123** 247402

[103] Okada M *et al* 2018 Direct and indirect interlayer excitons in a van der Waals heterostructure of $hBN/WS_2/MoS_2/hBN$ *ACS Nano* **12** 2498–505

[104] Kunstmann J *et al* 2018 Momentum-space indirect interlayer excitons in transition-metal dichalcogenide van der Waals heterostructures *Nat. Phys.* **14** 801–5

[105] Hanbicki A T, Chuang H-J, Rosenberger M R, Hellberg C S, Sivaram S V, McCreary K M, Mazin I I and Jonker B T 2018 Double indirect interlayer exciton in a $MoSe_2/WSe_2$ van der Waals heterostructure *ACS Nano* **12** 4719–26

[106] Miller B, Steinhoff A, Pano B, Klein J, Jahnke F, Holleitner A and Wurstbauer U 2017 Long-lived direct and indirect interlayer excitons in van der Waals heterostructures *Nano Lett.* **17** 5229–37

[107] Hong X, Kim J, Shi S-F, Zhang Y, Jin C, Sun Y, Tongay S, Wu J, Zhang Y and Wang F 2014 Ultrafast charge transfer in atomically thin MoS_2/WS_2 heterostructures *Nat. Nanotechnol.* **9** 682–6

[108] Grancini G, Maiuri M, Fazzi D, Petrozza A, Egelhaaf H-J, Brida D, Cerullo G and Lanzani G 2013 Hot exciton dissociation in polymer solar cells *Nat. Mater.* **12** 29–33

[109] Jailaubekov A E *et al* 2013 Hot charge-transfer excitons set the time limit for charge separation at donor/acceptor interfaces in organic photovoltaics *Nat. Mater.* **12** 66–73

[110] Ceballos F, Bellus M Z, Chiu H-Y and Zhao H 2014 Ultrafast charge separation and indirect exciton formation in a MoS_2–$MoSe_2$ van der Waals heterostructure *ACS Nano* **8** 12717–24

[111] Jin C, Ma E Y, Karni O, Regan E C, Wang F and Heinz T F 2018 Ultrafast dynamics in van der Waals heterostructures *Nat. Nanotechnol.* **13** 994–1003

[112] Yu H, Wang Y, Tong Q, Xu X and Yao W 2015 Anomalous light cones and valley optical selection rules of interlayer excitons in twisted heterobilayers *Phys. Rev. Lett.* **115** 187002

[113] Palummo M, Bernardi M and Grossman J C 2015 Exciton radiative lifetimes in two-dimensional transition metal dichalcogenides *Nano Lett.* **15** 2794–800

[114] Ovesen S, Brem S, Linderälv C, Kuisma M, Korn T, Erhart P, Selig M and Malic E 2019 Interlayer exciton dynamics in van der Waals heterostructures *Commun. Phys.* **2** 23

[115] Heo H *et al* 2015 Interlayer orientation-dependent light absorption and emission in monolayer semiconductor stacks *Nat. Commun.* **6** 7372

[116] Choi C *et al* 2018 Enhanced interlayer neutral excitons and trions in trilayer van der Waals heterostructures *npj 2D Mater. Appl.* **2** 30

[117] Zhou H, Zhao Y, Tao W, Li Y, Zhou Q and Zhu H 2020 Controlling exciton and valley dynamics in two-dimensional heterostructures with atomically precise interlayer proximity *ACS Nano* **14** 4618–25

[118] Shi H, Yan R, Bertolazzi S, Brivio J, Gao B, Kis A, Jena D, Xing H G and Huang L 2013 Exciton dynamics in suspended monolayer and few-layer MoS_2 2D crystals *ACS Nano* **7** 1072–80

[119] Salehi S and Saffarzadeh A 2016 Atomic defect states in monolayers of MoS_2 and WS_2 *Surf. Sci.* **651** 215–21

[120] Lin Z, Yan H, Liu J and An Y 2019 Defects engineering monolayer $MoSe_2$ magnetic states for 2D spintronic device *J. Alloys Compd.* **774** 160–7

[121] Nayak G *et al* 2019 Cathodoluminescence enhancement and quenching in type-I van der Waals heterostructures: cleanliness of the interfaces and defect creation *Phys. Rev. Mater.* **3** 114001

[122] Zheng S, So J-K, Liu F, Liu Z, Zheludev N and Fan H J 2017 Giant enhancement of cathodoluminescence of monolayer transitional metal dichalcogenides semiconductors *Nano Lett.* **17** 6475–80

[123] Cao Y, Fatemi V, Fang S, Watanabe K, Taniguchi T, Kaxiras E and Jarillo-Herrero P 2018 Unconventional superconductivity in magic-angle graphene superlattices *Nature* **556** 43–50

[124] He F, Zhou Y, Ye Z, Cho S-H, Jeong J, Meng X and Wang Y 2021 Moiré patterns in 2D materials: a review *ACS Nano* **15** 5944–58

[125] Li L, Wu M and Lu X 2023 Correlation, superconductivity and topology in graphene moiré superlattice *Front. Phys.* **18** 43401

[126] Jin C *et al* 2019 Observation of moiré excitons in WSe_2/WS_2 heterostructure superlattices *Nature* **567** 76–80

[127] Tran K *et al* 2019 Evidence for moiré excitons in van der Waals heterostructures *Nature* **567** 71–75

[128] Förg M, Baimuratov A S, Kruchinin S Y, Vovk I A, Scherzer J, Förste J, Funk V, Watanabe K, Taniguchi T and Högele A 2021 Moiré excitons in $MoSe_2$-WSe_2 heterobilayers and heterotrilayers *Nat. Commun.* **12** 1656

[129] Guo H, Zhang X and Lu G 2020 Shedding light on moiré excitons: a first-principles perspective *Sci. Adv.* **6** eabc5638

[130] Zhang L *et al* 2020 Twist-angle dependence of moiré excitons in $WS_2/MoSe_2$ heterobilayers *Nat. Commun.* **11** 5888

[131] Zhang L, Ni R and Zhou Y 2023 Controlling quantum phases of electrons and excitons in moiré superlattices *J. Appl. Phys.* **133** 080901

[132] Brem S, Linderälv C, Erhart P and Malic E 2020 Tunable phases of moiré excitons in van der Waals heterostructures *Nano Lett.* **20** 8534–40

[133] Lian Z *et al* 2023 Exciton superposition across moiré states in a semiconducting moiré superlattice *Nat. Commun.* **14** 5042

[134] Carr S, Massatt D, Fang S, Cazeaux P, Luskin M and Kaxiras E 2017 Twistronics: manipulating the electronic properties of two-dimensional layered structures through their twist angle *Phys. Rev.* B **95** 075420

[135] Liu Y, Zeng C, Yu J, Zhong J, Li B, Zhang Z, Liu Z, Wang Z M, Pan A and Duan X 2021 Moiré superlattices and related moiré excitons in twisted van der Waals heterostructures *Chem. Soc. Rev.* **50** 6401–22

[136] Kutana A, Penev E S and Yakobson B I 2014 Engineering electronic properties of layered transition-metal dichalcogenide compounds through alloying *Nanoscale* **6** 5820–5

[137] Li H *et al* 2014 Growth of alloy $MoS_{2x}Se_{2(1-x)}$ nanosheets with fully tunable chemical compositions and optical properties *J. Am. Chem. Soc.* **136** 3756–9

[138] Zhang W, Li X, Jiang T, Song J, Lin Y, Zhu L and Xu X 2015 CVD synthesis of $Mo_{(1-x)}W_xS_2$ and $MoS_{2(1-x)}Se_2x$ alloy monolayers aimed at tuning the bandgap of molybdenum disulfide *Nanoscale* **7** 13554–60

[139] Xi J, Zhao T, Wang D and Shuai Z 2014 Tunable electronic properties of two-dimensional transition metal dichalcogenide alloys: a first-principles prediction *J. Phys. Chem. Lett.* **5** 285–91

[140] Razeghizadeh M and Pourfath M 2022 First principles study on structural, electronic and optical properties of $HfS_{2(1-x)}Se_{2x}$ and $ZrS_{2(1-x)}Se_{2x}$ ternary alloys *RSC Adv.* **12** 14061–8

[141] Chen Y, Xi J, Dumcenco D O, Liu Z, Suenaga K, Wang D, Shuai Z, Huang Y-S and Xie L 2013 Tunable band gap photoluminescence from atomically thin transition-metal dichalcogenide alloys *ACS Nano* **7** 4610–6
[142] Deshpande A, Ratsch C, Ciobanu C V and Kodambaka S 2022 Entropy stabilization of two-dimensional transition metal dichalcogenide alloys: a density functional theory study *J. Appl. Phys.* **131** 234302
[143] Nugera F A, Sahoo P K, Xin Y, Ambardar S, Voronine D V, Kim U J, Han Y, Son H and Gutiérrez H R 2022 Bandgap engineering in 2D lateral heterostructures of transition metal dichalcogenides via controlled alloying *Small* **18** 2106600
[144] Lu A-Y *et al* 2017 Janus monolayers of transition metal dichalcogenides *Nat. Nanotechnol.* **12** 744–9
[145] Trivedi D B *et al* 2020 Room-temperature synthesis of 2D Janus crystals and their heterostructures *Adv. Mater.* **32** 2006320
[146] Zheng T, Lin Y-C, Rafizadeh N, Geohegan D B, Ni Z, Xiao K and Zhao H 2022 Janus monolayers for ultrafast and directional charge transfer in transition metal dichalcogenide heterostructures *ACS Nano* **16** 4197–205
[147] Chen F, Wang L and Ji X 2018 Evolution of two-dimensional $Mo_{1-x}W_{xS_2}$ alloy-based vertical heterostructures with various composition ranges via manipulating the Mo/W precursors *J. Phys. Chem.* C **122** 28337–46
[148] Yu S H *et al* 2014 Dye-sensitized MoS_2 photodetector with enhanced spectral photoresponse *ACS Nano* **8** 8285–91
[149] Maiti S, Poonia D, Schiettecatte P, Hens Z, Geiregat P, Kinge S and Siebbeles L D 2021 Generating triplets in organic semiconductor tetracene upon photoexcitation of transition metal dichalcogenide ReS_2 *J. Phys. Chem. Lett.* **12** 5256–60
[150] Jariwala D, Sangwan V K, Wu C-C, Prabhumirashi P L, Geier M L, Marks T J, Lauhon L J and Hersam M C 2013 Gate-tunable carbon nanotube–MoS_2 heterojunction p-n diode *Proc. Natl Acad. Sci.* **110** 18076–80
[151] Kufer D, Nikitskiy I, Lasanta T, Navickaite G, Koppens F H and Konstantatos G 2015 Hybrid 2D–0D MoS_2–PbS quantum dot photodetectors *Adv. Mater.* **27** 176–80
[152] Prins F, Goodman A J and Tisdale W A 2014 Reduced dielectric screening and enhanced energy transfer in single-and few-layer MoS_2 *Nano Lett.* **14** 6087–91
[153] Asaithambi A, Kazemi Tofighi N, Curreli N, De Franco M, Patra A, Petrini N, Baranov D, Manna L, Stasio F D and Kriegel I 2022 Generation of free carriers in $MoSe_2$ monolayers via energy transfer from $CsPbBr_3$ nanocrystals *Adv. Opt. Mater.* **10** 2200638
[154] Kovalenko M V, Protesescu L and Bodnarchuk M I 2017 Properties and potential optoelectronic applications of lead halide perovskite nanocrystals *Science* **358** 745–50
[155] Hong K, Van Le Q, Kim S Y and Jang H W 2018 Low-dimensional halide perovskites: review and issues *J. Mater. Chem.* **6** 2189–209
[156] Zhao Y and Zhu K 2016 Organic–inorganic hybrid lead halide perovskites for optoelectronic and electronic applications *Chem. Soc. Rev.* **45** 655–89
[157] Huang H, Bodnarchuk M I, Kershaw S V, Kovalenko M V and Rogach A L 2017 Lead halide perovskite nanocrystals in the research spotlight: stability and defect tolerance *ACS Energy Lett.* **2** 2071–83
[158] Akkerman Q A, Rainò G, Kovalenko M V and Manna L 2018 Genesis, challenges and opportunities for colloidal lead halide perovskite nanocrystals *Nat. Mater.* **17** 394–405
[159] Møller C K 1958 Crystal structure and photoconductivity of caesium plumbohalides *Nature* **182** 1436–1436
[160] Weber D 1978 $CH_3NH_3PbX_3$, ein Pb (II)-system mit kubischer perowskitstruktur/$CH_3NH_3PbX_3$, a Pb (II)-system with cubic perovskite structure *Z. Naturforsch.* B **33** 1443–5
[161] Mannino G, Deretzis I, Smecca E, La Magna A, Alberti A, Ceratti D and Cahen D 2020 Temperature-dependent optical band gap in $CsPbBr_3$, $MAPbBr_3$ and $FAPbBr_3$ single crystals *J. Phys. Chem. Lett.* **11** 2490–6
[162] Mannino G, Deretzis I, Smecca E, Giannazzo F, Valastro S, Fisicaro G, La Magna A, Ceratti D and Alberti A 2021 $CsPbBr_3$, $MAPbBr_3$ and $FAPbBr_3$ bromide perovskite single crystals: interband critical points under dry N_2 and optical degradation under humid air *J. Phys. Chem.* C **125** 4938–45
[163] Dolzhenko Y I, Inabe T and Maruyama Y 1986 *In situ* x-ray observation on the intercalation of weak interaction molecules into perovskite-type layered crystals $(C_9H_{19}NH_3)_2PbI_4$ and $(C_10H_{21}NH_3)_2CdCl_4$ *Bull. Chem. Soc. Japan* **59** 563–7
[164] Ishihara T, Takahashi J and Goto T 1990 Optical properties due to electronic transitions in two-dimensional semiconductors $(C_nH_{2n+1}NH_3)_2PbI_4$ *Phys. Rev.* B **42** 11099
[165] Protesescu L, Yakunin S, Bodnarchuk M I, Krieg F, Caputo R, Hendon C H, Yang R X, Walsh A and Kovalenko M V 2015 Nanocrystals of cesium lead halide perovskites ($CsPbX_3$, X = Cl, Br, and I): novel optoelectronic materials showing bright emission with wide color gamut *Nano Lett.* **15** 3692–6
[166] Zhang C, Zhang Y, Fang Z, Chen Y, Chen Z, He H and Zhu H 2021 Near-unity-efficiency energy transfer from perovskite to monolayer semiconductor through long-range migration and asymmetric interfacial transfer *ACS Appl. Mater. Interfaces* **13** 41895–903
[167] Zhang C, Lu G, Zhang Y, Fang Z, He H and Zhu H 2022 Long-range transport and ultrafast interfacial charge transfer in perovskite/monolayer semiconductor heterostructure for enhanced light absorption and photocarrier lifetime *J. Chem. Phys.* **156** 244701
[168] Van Der Laan M *et al* 2021 Photon recycling in $CsPbBr_3$ all-inorganic perovskite nanocrystals *ACS Photonics* **8** 3201–8
[169] Kang D-H, Pae S R, Shim J, Yoo G, Jeon J, Leem J W, Yu J S, Lee S, Shin B and Park J-H 2016 An ultrahigh-performance photodetector based on a perovskite–transition-metal-dichalcogenide hybrid structure *Adv. Mater.* **28** 7799–806
[170] Cheng H-C, Wang G, Li D, He Q, Yin A, Liu Y, Wu H, Ding M, Huang Y and Duan X 2016 van der Waals heterojunction devices based on organohalide perovskites and two-dimensional materials *Nano Lett.* **16** 367–73
[171] Peng B *et al* 2016 Achieving ultrafast hole transfer at the monolayer MoS_2 and $CH_3NH_3PbI_3$ perovskite interface by defect engineering *ACS Nano* **10** 6383–91
[172] Lu J, Carvalho A, Liu H, Lim S X, Castro Neto A H and Sow C H 2016 Hybrid bilayer WSe_2–$CH_3NH_3PbI_3$ organolead halide perovskite as a high-performance photodetector *Angew. Chem.* **128** 12124–8
[173] Gu X, Cui W, Li H, Wu Z, Zeng Z, Lee S-T, Zhang H and Sun B 2013 A solution-processed hole extraction layer made from ultrathin MoS_2 nanosheets for efficient organic solar cells *Adv. Energy Mater.* **3** 1262–8
[174] Bauer J, Quintanar L S, Wang K, Puretzky A A, Xiao K, Geohegan D B and Boulesbaa A 2018 Ultrafast exciton dissociation at the 2D-WS_2 monolayer/perovskite interface *J. Phys. Chem.* C **122** 28910–7
[175] Wu H, Kang Z, Zhang Z, Zhang Z, Si H, Liao Q, Zhang S, Wu J, Zhang X and Zhang Y 2018 Interfacial charge behavior modulation in perovskite quantum dot-monolayer MoS_2 0D-2D mixed-dimensional van der Waals heterostructures *Adv. Funct. Mater.* **28** 1802015
[176] Song X *et al* 2018 Boosting two-dimensional MoS_2/$CsPbBr_3$ photodetectors via enhanced light absorbance and interfacial carrier separation *ACS Appl. Mater. Interfaces* **10** 2801–9
[177] Bai F, Qi J, Li F, Fang Y, Han W, Wu H and Zhang Y 2018 A high-performance self-powered photodetector based on

monolayer MoS_2/perovskite heterostructures *Adv. Mater. Interfaces* **5** 1701275
[178] Noh T, Shin H S, Seo C, Kim J Y, Youn J, Kim J, Lee K-S and Joo J 2019 Significant enhancement of photoresponsive characteristics and mobility of MoS_2-based transistors through hybridization with perovskite $CsPbBr_3$ quantum dots *Nano Res.* **12** 405–12
[179] Xu Q, Yang Z, Peng D, Xi J, Lin P, Cheng Y, Liu K and Pan C 2019 Ws2/$CsPbBr_3$ van der Waals heterostructure planar photodetectors with ultrahigh on/off ratio and piezo-phototronic effect-induced strain-gated characteristics *Nano Energy* **65** 104001
[180] Das S, Ghorai A, Pal S, Mahato S, Das S and Ray S K 2023 Photosensitive field-effect transistor with enhanced photoamplification mediated by charge transfer in a heterostructure of α-$CsPbI_3$ nanocrystals and two-dimensional WS_2 *Phys. Rev. Appl.* **19** 034051
[181] Wu H, Si H, Zhang Z, Kang Z, Wu P, Zhou L, Zhang S, Zhang Z, Liao Q and Zhang Y 2018 All-inorganic perovskite quantum dot-monolayer MoS_2 mixed-dimensional van der Waals heterostructure for ultrasensitive photodetector *Adv. Sci.* **5** 1801219
[182] Kim M *et al* 2022 Perovskite quantum dot-induced monochromatization for broadband photodetection of wafer-scale molybdenum disulfide *NPG Asia Mater.* **14** 89
[183] Fang Q *et al* 2018 Ultrafast charge transfer in perovskite nanowire/2D transition metal dichalcogenide heterostructures *J. Phys. Chem. Lett.* **9** 1655–62
[184] Li H, Zheng X, Liu Y, Zhang Z and Jiang T 2018 Ultrafast interfacial energy transfer and interlayer excitons in the monolayer WS_2/$CsPbBr_3$ quantum dot heterostructure *Nanoscale* **10** 1650–9
[185] Wu H, Kang Z, Zhang Z, Si H, Zhang S, Zhang Z, Liao Q and Zhang Y 2019 Ligand engineering for improved all-inorganic perovskite quantum dot-MoS_2 monolayer mixed dimensional van der Waals phototransistor *Small Methods* **3** 1900117
[186] Grimaldi G, Van Den Brom M J, Du Fossé I, Crisp R W, Kirkwood N, Gudjonsdottir S, Geuchies J J, Kinge S, Siebbeles L D and Houtepen A J 2019 Engineering the band alignment in QD heterojunction films via ligand exchange *J. Phys. Chem.* C **123** 29599–608
[187] Zhang Q, Linardy E, Wang X and Eda G 2020 Excitonic energy transfer in heterostructures of quasi-2D perovskite and monolayer WS_2 *ACS Nano* **14** 11482–9
[188] Adhikari S *et al* 2020 Bandgap renormalization in monolayer MoS_2 on $CsPbBr_3$ quantum dots via charge transfer at room temperature *Adv. Mater. Interfaces* **7** 2000835
[189] Mu H, Tang J, Wang R, Qian M and Guo Q 2023 Exciton dynamics and photoresponse of a CVD-grown WS_2/thermally evaporated $CsSnBr_3$ heterostructure *J. Mater. Chem.* **11** 10310–23
[190] He J, Kumar N, Bellus M Z, Chiu H-Y, He D, Wang Y and Zhao H 2014 Electron transfer and coupling in graphene–tungsten disulfide van der Waals heterostructures *Nat. Commun.* **5** 5622
[191] Chen Y, Liu Z, Li J, Cheng X, Ma J, Wang H and Li D 2020 Robust interlayer coupling in two-dimensional perovskite/monolayer transition metal dichalcogenide heterostructures *ACS Nano* **14** 10258–64
[192] Wang Q *et al* 2020 Optoelectronic properties of a van der Waals WS_2 monolayer/2D perovskite vertical heterostructure *ACS Appl. Mater. Interfaces* **12** 45235–42
[193] Yang A *et al* 2019 Giant enhancement of photoluminescence emission in WS_2-two-dimensional perovskite heterostructures *Nano Lett.* **19** 4852–60
[194] Wang S, Luo Q, Fang W-H and Long R 2019 Interfacial engineering determines band alignment and steers charge separation and recombination at an inorganic perovskite quantum dot/WS_2 junction: a time domain *ab initio* study *J. Phys. Chem. Lett.* **10** 1234–41
[195] Liao C-S, Zhao Q-Q, Zhao Y-Q, Yu Z-L, Zhou H, He P-B, Yang J-L and Cai M-Q 2019 First-principles investigations of electronic and optical properties in the MoS_2/$CsPbBr_3$ heterostructure *J. Phys. Chem. Solids* **135** 109060
[196] Xu D-H, Liu J-F, Wan X-J, Liu X-Y, Cui G and Li L 2021 Theoretical study on the contacting interface-dependent band alignments of $CsPbBr_3$@ MoS_2 van der Waals heterojunctions: spin–orbit coupling does matter *J. Phys. Chem.* C **125** 21678–88
[197] Huang L, Huo N, Zheng Z, Dong H and Li J 2020 Two-dimensional transition metal dichalcogenides for lead halide perovskites-based photodetectors: band alignment investigation for the case of $CsPbBr_3$/$MoSe_2$ *J. Semicond.* **41** 052206
[198] He J, Su J, Lin Z, Zhang S, Qin Y, Zhang J, Chang J and Hao Y 2019 Theoretical studies of electronic and optical behaviors of all-inorganic $CsPbI_3$ and two-dimensional MS_2 (M = Mo, W) heterostructures *J. Phys. Chem.* C **123** 7158–65
[199] Wang D *et al* 2018 Bandgap broadening at grain boundaries in single-layer MoS_2 *Nano Res.* **11** 6102–9
[200] Rhodes D, Chae S H, Ribeiro-Palau R and Hone J 2019 Disorder in van der Waals heterostructures of 2D materials *Nat. Mater.* **18** 541–9
[201] Azizi A *et al* 2015 Freestanding van der Waals heterostructures of graphene and transition metal dichalcogenides *ACS Nano* **9** 4882–90
[202] Zhang W *et al* 2014 Ultrahigh-gain photodetectors based on atomically thin graphene-MoS_2 heterostructures *Sci. Rep.* **4** 3826
[203] Terrones H *et al* 2014 New first order Raman-active modes in few layered transition metal dichalcogenides *Sci. Rep.* **4** 4215
[204] Zhang W, Huang J-K, Chen C-H, Chang Y-H, Cheng Y-J and Li L-J 2013 High-gain phototransistors based on a CVD MoS_2 monolayer *Adv. Mater.* **25** 3456–61
[205] Kufer D and Konstantatos G 2015 Highly sensitive, encapsulated MoS_2 photodetector with gate controllable gain and speed *Nano Lett.* **15** 7307–13
[206] Zhao W, Ghorannevis Z, Chu L, Toh M, Kloc C, Tan P-H and Eda G 2013 Evolution of electronic structure in atomically thin sheets of WS_2 and WSe_2 *ACS Nano* **7** 791–7
[207] Zhao W, Ribeiro R M, Toh M, Carvalho A, Kloc C, Castro Neto A and Eda G 2013 Origin of indirect optical transitions in few-layer MoS_2, WS_2 and WSe_2 *Nano Lett.* **13** 5627–34
[208] Molas M R, Nogajewski K, Slobodeniuk A O, Binder J, Bartos M and Potemski M 2017 The optical response of monolayer, few-layer and bulk tungsten disulfide *Nanoscale* **9** 13128–41